THE ASTROPHYSICAL JOURNAL, 507:417–432, 1998 November 1

FLUX-TUBE TWIST RESULTING FROM HELICAL TURBULENCE: THE Σ-EFFECT

D. W. LONGCOPE,[1,2] G. H. FISHER,[3] AND A. A. PEVTSOV[1]

Received 1998 January 27; accepted 1998 June 8

ABSTRACT

Recent observational studies suggest that active region magnetic flux emerges in a twisted state and that the sense of twist depends weakly on solar hemisphere. We propose that this twist is imparted to the flux through its interaction with turbulent velocities in the convection zone. This process, designated the Σ-effect, operates on isolated magnetic flux tubes subjected to buffeting by turbulence with a nonvanishing kinetic helicity $\langle \boldsymbol{u} \cdot \nabla \times \boldsymbol{u} \rangle$. The Σ-effect leads to twist of the same sense inferred from observation and opposite to that predicted by the α-effect. A series of numerical calculations are performed to estimate the magnitude of the Σ-effect in the solar convective zone. The results compare favorably with observations in both mean value and statistical dispersion. We find a further relationship with total magnetic flux that can be tested in future observations. The model also predicts that twist is uncorrelated with the tilt angle of the active region.

Subject headings: MHD — plasmas — Sun: magnetic fields

1. INTRODUCTION

A number of recent observational studies of the solar magnetic field have begun to reveal trends in its handedness, or chirality. The chirality of the magnetic field has been inferred by a number of means including the morphology of filaments (Martin, Billamoria, & Tracadas 1994), morphology of coronal loops (Rust & Kumar 1996), in situ measurements of flux ropes (Burlaga 1988), and interplanetary fields (Bieber, Evenson, & Matthaeus 1987). Each of these methods reveals a tendency for chirality of one sense in the northern hemisphere and the opposite sense in the southern hemisphere. The tendency appears with different degrees of dominance in the different studies. The cause of this hemispheric tendency is still uncertain and is the topic of this work.

Pevtsov, Canfield, & Metcalf (1995, hereafter PCM) inferred the handedness of active region magnetic fields using vector magnetogram measurements. Maps of all three components of the magnetic field at a single height z can be used to calculate the vertical component of the electric current density

$$J_z(x, y, z = 0) = \left| \left(\frac{\partial B_y}{\partial x} - \frac{\partial B_x}{\partial y} \right) \right|_{z=0} ,$$

where x and y are the horizontal coordinates. Averaging the ratio J_z/B_z over an active region leads to a quantity characterizing chirality

$$\alpha_{\rm pcm} \equiv \left\langle \frac{J_z}{B_z} \right\rangle = \left\langle \frac{1}{B_z} \left(\frac{\partial B_y}{\partial x} - \frac{\partial B_x}{\partial y} \right) \right\rangle . \quad (1)$$

This quantity is referred to as "helicity" in PCM, but here we will call it *twist*. The definition of $\alpha_{\rm pcm}$ is motivated by analogy to a force-free magnetic field $\nabla \times \boldsymbol{B} = \alpha \boldsymbol{B}$. In fact, $\alpha_{\rm pcm}$ is a direct measure of the relative signs of the vertical current and flux at the photosphere. A positive value corresponds to field lines that twist in a right-handed sense as they cross the photosphere.

Pevtsov, Canfield, & Metcalf measured $\alpha_{\rm pcm}$ for 245 magnetograms of 69 different active regions (PCM). The vector magnetograms were measured with the Haleakala Stokes Polarimeter (Mickey 1985) between 1991 and 1995. An extended data set, using 203 active regions, is shown in Figure 1. It indicates a small but statistically significant tendency for left-handed twist ($\alpha_{\rm pcm} < 0$) in the northern hemisphere and right-handed twist in the southern hemisphere. This is consistent with trends in chirality inferred by other means (Zirker et al. 1997) but is by far the least pronounced tendency among these. The dispersion about the trend can be quantified by the rms departure from the linear trend, $\Delta\alpha_{\rm pcm} \simeq 1.28 \times 10^{-8}\ {\rm m}^{-1}$.

The PCM data set may provide insight into the state of flux prior to its emergence, insight not provided by other morphological or interplanetary estimates of chirality. The use of photospheric measurements to probe the subphotospheric field was explored by Leka et al. (1996) in an earlier study. They obtained vector magnetograms, using the Imaging Vector Magnetograph (Mickey et al. 1996), to follow the evolution of several emerging active regions. These revealed that as an active region emerged, and its net unsigned flux increased, the net unsigned vertical current increased as well. In fact, these two quantities were roughly proportional throughout the process of emergence. This led Leka et al. to conclude that the active region was carrying current prior to its emergence. In other words, the twist in the active region field was present in the flux below the photosphere. By extension, we believe that the $\alpha_{\rm pcm}$ from the PCM survey reflects a twist in subphotospheric flux and that the sense of twist has a hemispheric tendency.

We seek a theoretical model explaining the origin of twist in subphotospheric magnetic flux tubes. Such a model must predict values of $\alpha_{\rm pcm}$ with a hemispheric tendency, on top of a large degree of statistical scatter (dispersion) $\Delta\alpha_{\rm pcm}$. The origin of the hemispheric tendency is most likely related to solar rotation, either directly (e.g., through the Coriolis force) or indirectly (e.g., through differential rotation or kinetic helicity).

Emerging flux is deflected by the Coriolis force causing a "tilt" (relative to east-west) in the observed bipole, known as Joy's law. It has recently been shown (Longcope & Klapper 1997, hereafter LK) that this tilt will twist the field

[1] Department of Physics, Montana State University, Bozeman, MT 59717.
[2] Visiting Research Physicist, Space Sciences Laboratory, UC Berkeley.
[3] Space Sciences Laboratory, University of California, Berkeley, CA 94720.

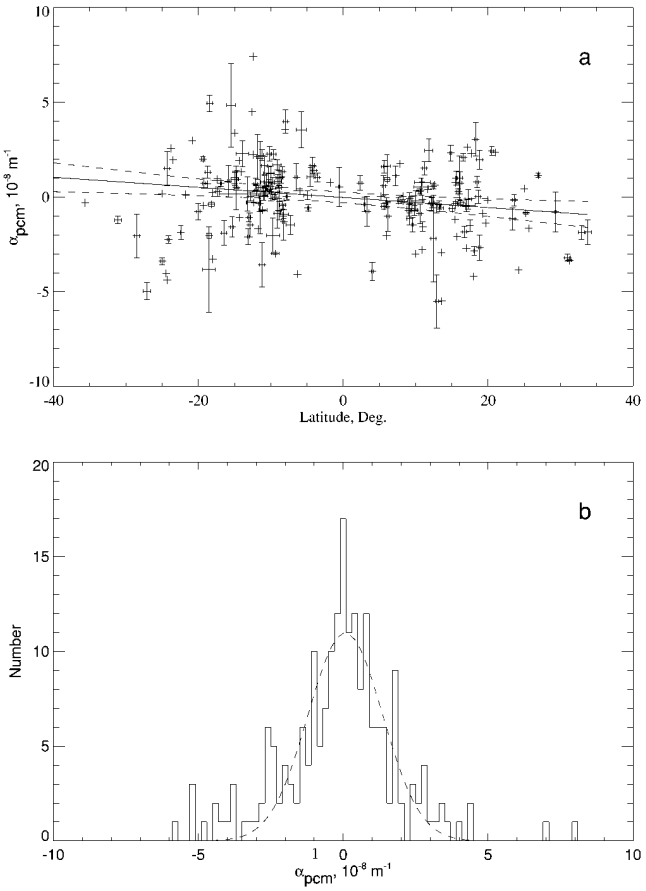

FIG. 1.—Measured values of α_{pcm} for 203 active regions. (*a*) α_{pcm} plotted against the solar latitude of the active region. Error bars denote the variations in different observations of the same active region. A linear fit to the data (*solid line*) $\alpha_{pcm} = -2.7 \times 10^{-10}\theta_{deg}$ m^{-1} and the 2 σ errors (*dashed lines*) reveal the hemispheric tendency. (*b*) A histogram of the data after the linear fit has been subtracted. The dashed curve is a Gaussian with zero mean (the fit has been removed) and a width $\Delta\alpha_{pcm} = 1.28 \times 10^{-8}$ m^{-1}.

lines within the flux tube. Longcope & Klapper predict values

$$\alpha_{pcm} \simeq -\frac{\pi^3 |\psi| \psi}{4d}, \qquad (2)$$

where d is the polar separation and ψ is the tilt angle (in radians) defined to be positive (negative) in the northern (southern) hemisphere when adhering to Joy's law. According to this model, the Coriolis force leads to a value of α_{pcm} with the correct sign. This theoretical calculation neglected the possible propagation of twist, as torsional Alfvén waves, during emergence. Propagation would only decrease the value in equation (2), which presently predicts values just a bit too small: $\alpha_{pcm} = -2 \times 10^{-9}$ m^{-1} ($\psi = 10°$ and $d = 100$ Mm). Nor is the dominant statistical scatter accounted for by this model.

In addition to a large-scale tilt, the flux tube will accumulate random distortions from the convection zone (CZ) turbulence. This can give rise to twist through a mechanism we call the Σ-effect. Turbulence in the solar CZ is believed to possess a nonvanishing *kinetic helicity* $\langle \boldsymbol{u} \cdot \nabla \times \boldsymbol{u} \rangle$ (see § 4.1). There is a hemispheric dependence in the kinetic helicity, due ultimately to the Coriolis force acting on the turbulent fluid. We will model the interaction of CZ turbulence with the rising flux tube to demonstrate that the Σ-effect results in a value of α_{pcm} consistent with values found by PCM. The large amount of statistical dispersion will occur naturally in a process driven by turbulence.

The emergence of an active region has been successfully modeled as the buoyant rise of an isolated magnetic flux tube (Parker 1975). A nonlinear set of dynamical equations for a buoyant flux tube was proposed by Spruit (1981) and has been improved and applied by subsequent investigators. This model has successfully predicted, and observations have confirmed, the Joy's law relationship between ψ and solar latitude θ (D'Silva & Choudhuri 1993; Caligari, Moreno-Insertis, & Schüssler 1995), as well as separate relationships between ψ and total active region flux Φ (Fan, Fisher, & McClymont 1994; Fisher, Fan, & Howard 1995) and between the statistical dispersion $\Delta\psi$ and active region flux Φ. The first two relationships result from the Coriolis force acting on the rising, expanding tube. The last relationship was studied by Longcope & Fisher (1996, hereafter LF) by considering the effect of convection zone turbulence on a nearly horizontal flux tube.

Recently, the possible effect of twist on the dynamics of thin-flux tubes has been investigated (Ferriz-Mas & Schüssler 1990; Chui & Moffatt 1995). In particular, the nonlinear dynamical flux tube equations of Spruit have been generalized to include the twisted magnetic field within the tube (LK). The theoretical relation in equation (2) between tilt angle ψ and α_{pcm} is found using these model equations. This explanation, however, seems inadequate for the data in Figure 1, for reasons described earlier.

In this work the same twisted flux tube equations are used to explore the effect of turbulence on the generation and evolution of flux tube twist. As in LF, a nearly straight, horizontal tube is buffeted by a random velocity field, representing the CZ turbulence. The random velocity field is assumed to have a nonzero kinetic helicity, $\langle \boldsymbol{u} \cdot \nabla \times \boldsymbol{u} \rangle$, as is believed to be the case in CZ turbulence. We show below that the kinetic helicity gives the flux tube distortions of a roughly helical nature. This leads, in turn, to a net twist in the field lines: the Σ-effect.

While the end result resembles that of the α-effect in mean field electrodynamics (Moffatt 1978; Krause & Rädler 1981), the Σ-effect is different in several important respects. First, no dissipation or turbulent diffusion is necessary in the Σ-effect, nor is magnetic helicity changed. Second, the Σ-effect occurs in tubes with a strong magnetic field, while the α-effect is believed to be "quenched" by a significant Lorentz restoring force (Bhattacharjee & Yuan 1995). Most importantly, the sign of the Σ-effect is *opposite* that of the α-effect, and thus it agrees with the hemispheric tendency of PCM.

We perform quantitative calculations to estimate the magnitude of twist resulting from the Σ-effect. The magnitudes found are consistent with those from PCM. In addition to an average twist $\langle \alpha_{pcm} \rangle$, scaling roughly linearly with solar latitude, there is a statistical dispersion $\Delta\alpha_{pcm}$ whose magnitude can be 10 times greater than the mean; this is also consistent with observations from PCM (see Fig. 1). We find a further relationship between $\langle \alpha_{pcm} \rangle$ and the flux of the tube Φ; evidence of this relationship can be sought in future observations. Finally, we find no significant correlation between the twist and the bipolar tilt angle ψ.

The next section presents the dynamical equations for the evolution of the axis of a nearly straight rising flux tube. These equations are the same for twisted or untwisted flux

tubes. Section 3 introduces flux tube twist as described by Longcope & Klapper (LK). This leads to an extended set of dynamical equations that include the Σ-effect. In the full set of dynamical equations the turbulent velocity appears as an external driving term. Section 4 presents a model for this driving term based on properties of turbulent velocity in the CZ, including its kinetic helicity. In § 5 this model turbulence is applied to the dynamical equations from §§ 2 and 3 to yield numerical values for $\alpha_{\rm pcm}$.

2. THE RISE OF A NEARLY STRAIGHT FLUX TUBE

A thin-flux tube can be described as a curve in space, $\boldsymbol{r}(\ell)$, parameterized by distance, ℓ, along itself. The instantaneous velocity of a tube element is denoted by the vector $\boldsymbol{u} = (u, v, w)$ while the velocity of the external medium at the same point is denoted by $\boldsymbol{u}^e = (u^e, v^e, w^e)$. An equation for that component of the velocity perpendicular to the tube's local tangent is (Spruit 1981; Choudhuri & Gilman 1987)

$$\frac{d}{dt}\boldsymbol{u}_\perp = \frac{\delta\rho}{2\rho}\, g(\hat{\boldsymbol{t}}\times\hat{\boldsymbol{z}})\times\hat{\boldsymbol{t}} + \frac{1}{2}\, v_{\rm A}^2\,\boldsymbol{\kappa} - \frac{C_D}{2\pi a}\,|\boldsymbol{u}_\perp - \boldsymbol{u}_\perp^e|\,(\boldsymbol{u}_\perp - \boldsymbol{u}_\perp^e)\,, \tag{3}$$

where a is the radius of the tube's cross section and C_D is the coefficient of aerodynamic drag. The local tangent vector, $\hat{\boldsymbol{t}}$, and curvature vector, $\boldsymbol{\kappa}$, are defined as

$$\hat{\boldsymbol{t}} \equiv \frac{\partial \boldsymbol{r}}{\partial \ell}\,, \quad \boldsymbol{\kappa} \equiv \frac{\partial^2 \boldsymbol{r}}{\partial \ell^2}\,.$$

The total time derivative is taken in a frame following the local tube element. The vertical coordinate, z, increases downward, denoting depth beneath the photosphere. The coordinate system is right-handed.

This equation describes the acceleration of each section of the tube due to the various forces acting on it. The first term on the right-hand side of equation (3) represents the buoyancy force. The difference between internal and external mass densities, $\delta\rho \equiv \rho^i - \rho^e$, is assumed to be much smaller than either of them: $\rho = \rho^e \simeq \rho^i$. Gravity acts with an acceleration $g = g(z)$ in the downward ($\hat{\boldsymbol{z}}$-) direction; in equation (3) the force is projected into the plane perpendicular to $\hat{\boldsymbol{t}}$. For a buoyant tube ($\delta\rho < 0$) the actual acceleration will be upward.

The second term represents the magnetic tension resulting in a net force in the direction of the tube's curvature, perpendicular to $\hat{\boldsymbol{t}}$. Its coefficient is the square of the wave speed of transverse *tube waves*

$$v_t \equiv \frac{B}{\sqrt{8\pi\rho}} = \frac{v_{\rm A}}{\sqrt{2}}\,, \tag{4}$$

where $B = \Phi/\pi a^2$ is the magnetic field strength of the tube. This speed is slower by a factor of $1/2^{1/2}$ than the speed of transverse Alfvén waves because of the effect of displacing external fluid (Ryutov & Ryutova 1976).

The final term represents the aerodynamic drag as the tube slips through the external medium (Parker 1975). At a high Reynolds number the coefficient of drag approaches a limit of order unity (Batchelor 1967); for simplicity we will henceforth take $C_D = 1$.

The Coriolis force has been neglected in equation (3) in order to study the Σ-effect in isolation from other sources of flux tube twist. In a flux tube rising as an Ω-loop the Coriolis force tilts the apex giving rise to Joy's law. This tilt gives rise, in turn, to the twist calculated by LK. In the present work, however, we seek *an alternative* source of twist, arising not from Joy's law, but from turbulence. To do this we consider a strictly horizontal flux tube, not an Ω-loop. Joy's law does not occur in such a configuration, nor can the Coriolis force be introduced self-consistently.

Notably missing are any forces related to twist of the magnetic field within the tube. Equation (3) was originally proposed for untwisted flux tubes, i.e., tubes in which all field lines were parallel to the axis $\boldsymbol{r}(s)$. Recently, the equations were generalized to include the effect of twisted flux (LK). The additional terms resulting from twist were found to be smaller than those in equation (3) by a factor of $\sim a^2/L_w^2$, where L_w is the axial distance over which a field line wraps once about the axis (Ferriz-Mas & Schüssler 1990; LK). If $a \ll L_w$, a limit known as *weak twist*, the effect of twist on the axial dynamics can be neglected and equation (3) can be used to solve for the evolution of the axis. The twist does not affect the axis, but it will be shown below that the axis *does* affect the twist. We will henceforth assume we are always in the weakly twisted limit.

In the absence of external flow ($\boldsymbol{u}^e = 0$) equation (3) admits a simple solution describing the rise of a perfectly straight horizontal flux tube:

$$\boldsymbol{r}_0(\ell) = [\ell,\, 0,\, z_0(t)]\,,$$

in Cartesian coordinates. The tube rises at a rate $v_{\rm ff}$ determined by the balance of buoyancy and aerodynamic drag

$$\dot{z}_0 = w_0 = -v_{\rm ff}(z_0) = -\left[\left|\frac{\delta\rho(z_0)}{\rho(z_0)}\right|\frac{g a(z_0)\pi}{C_D}\right]^{1/2}, \tag{5}$$

where the various properties of the tube, such as its radius a and its over-density $\delta\rho$, depend on depth. The details of this solution were presented in LF and are reviewed briefly in Appendix A. For the present, however, we will take $z_0(t)$ to be known. This in turn means that all properties of the tube can also be written as known functions of time: $a(t)$, $\delta\rho(t)$, and so on.

The external velocity can be introduced as a small perturbation giving rise to small changes $\boldsymbol{r}_1(x, t)$ in the straight, horizontal axis. At this order we have replaced the length coordinate ℓ by x, which is the length in the zeroth-order solution. The equation of motion (3) can be expanded to next order to give

$$\frac{\partial^2 y_1}{\partial t^2} + \frac{C_D v_{\rm ff}}{2\pi a}\frac{\partial y_1}{\partial t} - \frac{1}{2}\, v_{\rm A}^2\,\frac{\partial^2 y_1}{\partial x^2} = \frac{C_D v_{\rm ff}}{2\pi a}\,\tilde{v}^e(x, t)\,, \tag{6a}$$

$$\frac{\partial^2 z_1}{\partial t^2} + \frac{2C_D v_{\rm ff}}{2\pi a}\frac{\partial z_1}{\partial t} - \frac{1}{2}\, v_{\rm A}^2\,\frac{\partial^2 z_1}{\partial x^2} = \frac{2C_D v_{\rm ff}}{2\pi a}\,\tilde{w}^e(x, t)\,. \tag{6b}$$

The right-hand side consists of the perpendicular components of the external velocity evaluated at the position of the unperturbed axis

$$\tilde{v}^e(x, t) \equiv v^e[x,\, y = 0,\, z = z_0(t),\, t]\,, \tag{7a}$$

$$\tilde{w}^e(x, t) \equiv w^e[x,\, y = 0,\, z = z_0(t),\, t]\,. \tag{7b}$$

Equation (6b) neglects several terms involving gravity and parallel flow. These terms are the basis of the Parker instability, so they are arguably significant. On the other hand, the zeroth-order solution is meant to represent a tube

undergoing the Parker instability; by discarding such terms from the first-order equations we are trying to isolate the effects of turbulence from the rise itself.

Equations (6a) and (6b) are linear inhomogeneous equations for displacements from the horizontal. Solutions can be sought as a Fourier series

$$y_1(x, t) = \sum_k y_k(t) e^{ikx},\ \tilde{v}^e(x, t) = \sum_k \tilde{v}^e_k(t) e^{ikx}\ , \tag{8}$$

and likewise for $z_1(x, t)$ and $\tilde{w}^e(x, t)$. Replacing these in equations (6a) and (6b) leads to independent equations for each Fourier mode

$$\ddot{y}_k + \lambda \dot{y}_k + \tfrac{1}{2} v_{\rm A}^2 k^2 y_k = \lambda \tilde{v}^e_k(t)\ , \tag{9a}$$

$$\ddot{z}_k + 2\lambda \dot{z}_k + \tfrac{1}{2} v_{\rm A}^2 k^2 z_k = 2\lambda \tilde{w}^e_k(t)\ . \tag{9b}$$

These are equations for driven, damped harmonic oscillators. The damping coefficient is a function of time given by

$$\lambda \equiv \frac{C_D v_{\rm ff}}{2\pi a} = \left(\left| \frac{\delta\rho}{\rho} \right| \frac{g C_D}{4\pi a} \right)^{1/2}\ . \tag{10}$$

Horizontal perturbations with $k < k_{{\rm cr},\perp} \equiv \lambda / v_{\rm A}$ are overdamped. This critical wavenumber will change over time as the tube rises.

The tube is initialized to be perfectly straight, $y_k(t = 0) = z_k(t = 0) = 0$, and allowed to deform because of the influence of the external velocities. These velocities are due to turbulent convection and will be modeled as random noise. The properties of this noise derive from the properties of the turbulence surrounding the rising tube. The horizontal and vertical distortions will be correlated only in so far as the random driving velocities $\tilde{v}^e$ and $\tilde{w}^e$ are.

3. TWIST AND WRITHE

3.1. *Evolution of Twist in a Thin Tube*

The flux tube, whose axis is $\boldsymbol{r}(\ell)$, consists of individual field lines that twist about this axis. Within a given cross section of the tube each field line is assumed to twist with the same pitch $q(\ell)$ (positive for right-handed twist). In a locally cylindrical coordinate system, (ϖ, ϕ, ℓ), the tube's internal field must therefore be

$$(B_\varpi, B_\phi, B_\ell) \simeq (0, q\varpi B_\ell, B_\ell)\ , \tag{11}$$

where $B_\ell(\ell) = \Phi / [\pi a^2(\ell)]$. In addition to $\boldsymbol{u}$, the velocity of the tube's center, there is an internal spinning motion

$$(v_\varpi, v_\phi, v_\ell) \simeq (0, \omega\varpi, 0)\ , \tag{12}$$

where $\omega(\ell)$ is the angular frequency of spinning about the axis. Detailed definitions of $q(\ell)$ and $\omega(\ell)$ are presented by LK.

The twist $q(\ell)$ of field lines about the axis, is quite distinct from any twist that might be present in the axis itself. Figure 2 shows a horizontal flux tube whose axis is deformed into an Ω-loop with a left-handed sense of pitch. Such a twist might be caused by the Coriolis effect in the southern hemisphere of the Sun. Along the outside of the tube are shown representative field lines. In this example the field lines twist about the axis in a right-handed sense, in spite of the left-handed twist of the axis. We will show below that this is natural for a tube that is initially straight and untwisted.

One consequence of the twist $q(\ell)$ is an axial torque on any cross section of the tube. For a tube whose pitch is constant, the torques on each element balance. An axial variation in $q(\ell)$, however, leads to unbalanced torques causing the angular frequency ω to change according to

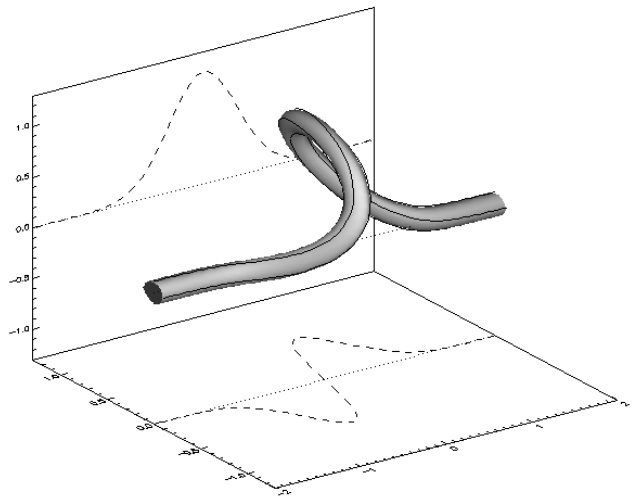

FIG. 2.—Horizontal flux tube whose axis $\boldsymbol{r}(\ell)$ is deformed into a left-handed Ω-loop. The field lines twist about the axis in the right-handed sense: $q(\ell) > 0$. The tube was initially straight and untwisted. The axis was distorted sufficiently rapidly that twist has not propagated to the ends.

$$\frac{d\omega}{dt} = -2a^{-1} \frac{da}{dt}\, \omega + v_{\rm A}^2 \frac{\partial q}{\partial \ell}\ . \tag{13}$$

The first term on the right-hand side arises from the changing moment of inertia of an expanding or contracting tube. The second term arises from torque imbalance. No mechanism has been included for the external flow to exert a torque directly on the tube. Such an effect would require some form of viscous stress on the surface of the tube; we ignore such a possibility.

Geometry alone dictates the time evolution of twist $q(\ell)$ of a flux tube or of a ribbon (Klapper & Tabor 1994). Accounting for the simultaneous influences of axis motion, as well as the spinning, yields

$$\frac{dq}{dt} = -\zeta q + \frac{\partial \omega}{\partial \ell} + \Sigma(\ell, t)\ . \tag{14}$$

The first term on the right-hand side accounts for a change in twist q as the axis stretches. The differential rate at which the axis stretches is

$$\zeta \equiv \frac{d \ln(\delta\ell)}{dt} = \hat{\boldsymbol{t}} \cdot \frac{\partial \boldsymbol{u}}{\partial \ell}\ . \tag{15}$$

The second term expresses the increase in twist if the two ends of a tube element are spinning differently. The third term,

$$\Sigma \equiv \left(\frac{\partial \hat{\boldsymbol{t}}}{\partial \ell} \times \frac{d\hat{\boldsymbol{t}}}{dt} \cdot \hat{\boldsymbol{t}} \right) = (\hat{\boldsymbol{t}} \times \boldsymbol{\kappa}) \cdot \frac{\partial \boldsymbol{u}}{\partial \ell}\ , \tag{16}$$

depends only on the configuration and evolution of the axis. It is the only term between equations (13) and (14) that is not linear in either ω or q; as such it can be considered the *source of twist*.

It may not be obvious how the motion of a tube's axis can twist the field lines that compose it. This is a purely geometrical effect, and it can be appreciated by considering

magnetic helicity. The magnetic helicity, $\mathscr{H}$, of a closed flux tube is a geometric quantity that is strictly conserved under any ideal plasma motion. It has been shown that for a thin-flux tube the helicity can be decomposed into a part involving local twist and a part involving only the axis (Berger & Field 1984; Moffatt & Ricca 1992)

$$\mathscr{H} \equiv \int \boldsymbol{A} \cdot \boldsymbol{B}\, dx = \frac{\Phi^2}{2\pi} (\mathrm{Tw} + \mathrm{Wr}) . \tag{17}$$

The total twist, Tw, is simply an integral of the local twist q

$$\mathrm{Tw} = \oint q(\ell) d\ell . \tag{18}$$

The writhe, Wr, represents a helicity contribution from the axis alone involving a double integral

$$\mathrm{Wr} = \frac{1}{2} \oint d\ell' \oint d\ell'' \frac{\hat{\boldsymbol{t}}' \times \hat{\boldsymbol{t}}'' \cdot (\boldsymbol{r}'' - \boldsymbol{r}')}{|\boldsymbol{r}'' - \boldsymbol{r}'|^3} , \tag{19}$$

where $\boldsymbol{r}' \equiv \boldsymbol{r}_1(\ell')$ and so on. (Conventional definitions of these quantities include a prefactor of $1/2\pi$.) By time differentiating Tw and using equation (14), the equation for $\dot{q}$, gives

$$\frac{d(\mathrm{Tw})}{dt} = \oint \left(\frac{dq}{dt} + \zeta q \right) d\ell = \oint \Sigma(\ell) d\ell = -\frac{d(\mathrm{Wr})}{dt} , \tag{20}$$

where we have used the fact that $d\mathscr{H}/dt = 0$. Remarkably, while Wr itself is a double integral, its time derivative is a single integral whose density is $-\Sigma$. This can also be verified (with some effort) by direct differentiation of equation (19). Thus $\Sigma(\ell)$ represents the *local* exchange of "writhe density" for twist density q.

The rate of extension, ζ, is related to the change in radius, a. Since the mass of a tube element, $\delta M = \pi a^2 \rho \delta \ell$, is conserved, we find

$$\frac{d \ln(\delta M)}{dt} = 0 = \frac{d \ln(a^2)}{dt} + \frac{d \ln(\rho)}{dt} + \frac{d \ln(\delta \ell)}{dt} .$$

This allows us to write

$$2a^{-1} \frac{da}{dt} = -\zeta + \frac{v_{\mathrm{ff}}}{\Lambda_\rho} , \tag{21}$$

where $\Lambda_\rho(z)$ is the density scale height at the present depth.

3.2. *A Nearly Straight Tube*

Applying equations (13) and (14) to the horizontal rising tube $\boldsymbol{r}_0$ we find $\Sigma = \zeta = 0$. This means that a tube may rise remaining untwisted: $q_0 = \omega_0 = 0$. Considering the perturbed tube, the terms ζ and Σ are both second order in small quantities:

$$\zeta(x, t) \simeq \frac{\partial \boldsymbol{r}_1}{\partial x} \cdot \frac{\partial \boldsymbol{u}_1}{\partial x} = \frac{\partial y_1}{\partial x} \frac{\partial v_1}{\partial x} + \frac{\partial z_1}{\partial x} \frac{\partial w_1}{\partial x} , \tag{22}$$

$$\Sigma(x, t) \simeq \hat{\boldsymbol{x}} \times \frac{\partial^2 \boldsymbol{r}_1}{\partial x^2} \cdot \frac{\partial \boldsymbol{u}_1}{\partial x} = \frac{\partial^2 y_1}{\partial x^2} \frac{\partial w_1}{\partial x} - \frac{\partial^2 z_1}{\partial x^2} \frac{\partial v_1}{\partial x} . \tag{23}$$

Since Σ is the source term it follows that both q and ω are also second-order quantities. To this order equations (13) and (14) can be rewritten

$$\frac{\partial \omega}{\partial t} = -\gamma_\rho \omega + v_{\mathrm{A}}^2 \frac{\partial q}{\partial x} , \tag{24a}$$

$$\frac{\partial q}{\partial t} = \frac{\partial \omega}{\partial x} + \Sigma(x, t) , \tag{24b}$$

where $\gamma_\rho \equiv v_{\mathrm{ff}}/\Lambda_\rho$ is a function of time through the depth dependence of v_{ff} and Λ_ρ. Expressing $q(x, t)$ and $\omega(x, t)$ as Fourier series with time-dependent coefficients yields

$$\dot{\omega}_k = -\gamma_\rho \omega_k + ikv_{\mathrm{A}}^2 q_k , \tag{25a}$$

$$\dot{q}_k = ik\omega_k + \Sigma_k . \tag{25b}$$

The source term can be expressed in terms of the Fourier coefficients of the axis perturbations

$$\Sigma_k = \sum_p ip^2(p - k)(y_p w_{k-p} - z_p v_{k-p}) . \tag{26}$$

Equations (25a) and (25b) are the equations for torsional Alfvén waves that propagate at v_{A} (added mass does not affect torsional motion). The waves damp at a rate γ_ρ because of the rise of the tube. In this sense Σ is a source term for torsional Alfvén waves.

The spatially averaged twist of the flux tube is given by the $k = 0$ component, q_0, for which the equation takes the much simpler form

$$\dot{q}_0 = \Sigma_0 = \sum_p ip^3(y_p w_p^* - z_p v_p^*) = -\frac{d}{dt} \sum_p p^3 \,\mathrm{Im}\,(y_p z_p^*) , \tag{27}$$

(any $k = 0$ Fourier coefficient must be purely real). This can be easily solved; if the tube is initially untwisted, $q_k(0) = 0$, the solution is

$$q_0 = -\sum_p p^3 \,\mathrm{Im}\,(y_p z_p^*) . \tag{28}$$

It is also possible to place the Fourier expansion of the nearly horizontal axis into equation (19) for writhe and find, to leading order,

$$\mathrm{Wr} = \int_{-\infty}^{\infty} \mathrm{Wr}_0' \, dx , \tag{29}$$

where the average writhe density is given by

$$\mathrm{Wr}_0' = \sum_p p^3 \,\mathrm{Im}\,(y_p z_p^*) . \tag{30}$$

The total writhe of the infinitely long flux tube diverges, as does the total twist. The average twist density in the tube naturally cancels out the average writhe density since the helicity of the tube must be zero.

The expression $\mathrm{Im}\,(y_p z_p^*)$ quantifies the helical nature of the axis in direct analogy to the circular polarization in a transverse wave (see, e.g., Jackson 1975, § 7.2). Consider an axis that forms a helix of right-handed pitch p and amplitude R

$$\boldsymbol{r}_1(x) = R[\cos(px)\hat{\boldsymbol{y}} + \sin(px)\hat{\boldsymbol{z}}] . \tag{31}$$

The Fourier coefficients for this case are simply $y_p = y_{-p} = \frac{1}{2}R$ and $z_p = -z_{-p} = -(i/2)R$. Placing these in equation (30) gives

$$\mathrm{Wr}_0' = \tfrac{1}{2} R^2 p^3 . \tag{32}$$

The writhe density of a helix is positive if it is right-handed, thus it will create negative (left-handed) twist in the field lines. If the axis were deformed into a helix from a straight untwisted tube then equation (28) gives

$$q_0 = -\tfrac{1}{2}R^2p^3 ,$$

in agreement with LK. An arbitrary axis $\boldsymbol{r}_1(x)$ can be decomposed into right-handed and left-handed helices of varying pitches, just as an arbitrary transverse wave packet can be decomposed into right and left circularly polarized components. According to equation (30), the writhe density is then the sum of the writhe densities of each helical component. The average twist is just the opposite of the writhe density.

Thus, a rising flux tube, initially untwisted, can be twisted by the action of turbulence if the final deformed axis has a net helical pitch. The axis is deformed through the action of random turbulence, so the Fourier coefficients y_k and z_k will be random. On average, there will be a net twist if there is some statistical correlation between these coefficients

$$\langle q_0 \rangle = -\sum_k k^3 \, \mathrm{Im} \, \langle y_k z_k^* \rangle , \tag{33}$$

where the averaging $\langle \cdots \rangle$ is over different realizations of the turbulent velocities. As noted above we can expect a statistical correlation between y_k and z_k only if there is such a correlation in the turbulent velocities $\tilde{v}_k^e$ and $\tilde{w}_k^e$. In particular, producing a nonvanishing value of Im $\langle y_k z_k^* \rangle$ requires that Im $\langle \tilde{v}_k^e \tilde{w}_k^{e*} \rangle$ be nonvanishing. This implies a "circular polarization" of the turbulent velocity, otherwise known as *kinetic helicity*.

Figure 3 shows the random perturbations to a model flux tube that has risen from the base of the CZ ($z = 200$ Mm) to a depth of $z = 160$ Mm. It has been subject to turbulence with Im $\langle \tilde{v}_k^e \tilde{w}_k^{e*} \rangle > 0$. It is apparent from Figures 3*b* and 3*d* that the axis of the tube has a right-handed sense of twist: positive writhe and Im $\langle y_k z_k^* \rangle > 0$.

3.3. *The α-Effect and the Σ-Effect*

We argue above that turbulence with nonvanishing kinetic helicity can cause the field lines in a flux tube to develop twist. By referring to equation (11) this twist corresponds to a component of the field, B_ϕ, which is locally azimuthal, relative to the primary axial component B_ℓ. In treatments of mean field electrodynamics it is customary to phrase this generation process in terms of the α-effect (Moffatt 1978; Krause & Rädler 1981). Specifically, the α-effect is a change in the axial component of the average *vector potential*

$$\frac{\partial \langle A_\ell \rangle}{\partial t} = -c\langle E_\ell \rangle = -\alpha \langle B_\ell \rangle , \tag{34}$$

where we omit the terms because of the mean velocities (i.e., shear). This definition is such that positive α twists the field in the right-handed sense. When applied to an isolated flux tube, however, this equation predicts an azimuthal field B_ϕ concentrated mostly at the tube's surface, where $B_\ell(\varpi)$ changes most rapidly. Equation (34) is derived for a magnetic field dominated by a smooth nonstatistical component that varies over large scales. It is not clear that this traditional analysis applies to an isolated tube with strong magnetic field (Bhattacharjee & Yuan 1995).

The twist in our flux tube is more directly related to the axial current density

$$J_\ell = \frac{1}{\varpi}\frac{\partial}{\partial \varpi}(\varpi B_\phi) = 2qB_\ell , \quad \varpi < a . \tag{35}$$

There is also a narrow layer of return current along the surface $\varpi = a$. In analogy to the α-effect we shall consider a change to J_ℓ due to the turbulence alone:

$$\frac{\partial \langle J_\ell \rangle}{\partial t} = 2\langle \dot{q} \rangle B_\ell = 2\langle \Sigma_0 \rangle B_\ell , \tag{36}$$

ignoring the return current layer. The final expression results from using equation (27), $\dot{q}_0 = \Sigma_0$, inside the averages. Thus, the effect of turbulence is to generate a current, rather than a vector potential; we refer to this as the Σ-effect. The coefficient is once again defined so that positive $\langle \Sigma_0 \rangle$ leads to right-handed twist.

It is important to note that $\langle \Sigma_0 \rangle > 0$ twists the field lines in the right-handed sense only because the axis is being twisted in the left-handed sense (see Fig. 2). Fluid motions with a right-handed sense will deform a flux tube in a left-handed sense (Moffatt 1978). This is expected in a rising, expanding flow, being acted on by the Coriolis force in the southern hemisphere of the Sun. That is to say, right-handed fluid motions produce left-handed *writhe* in the flux tube. This leads, by conservation of helicity, to right-handed *twist* and therefore to a value $\langle \Sigma_0 \rangle > 0$ in the southern hemisphere. Thus, the Σ-effect should produce $J/B > 0$ in the southern hemisphere (and $J/B < 0$ in the northern hemisphere). These relations, along with the hemispheric variations in related quantities, are summarized in Table 1.

We present this brief comparison with the α-effect simply because it is another well-known source of twist in MHD. In fact, the α-effect and the Σ-effect are very different phenomena. The α-effect relates the evolution of any magnetic field to the fluid velocity *within* that field; it is derived from the standard induction equation. The Σ-effect pertains only to magnetic field in the form of isolated flux tubes. It relates the evolution of the field inside the tube to the fluid velocity *outside* the tube. It follows only from global geometric constraints (i.e., magnetic helicity) after *assuming* a form for the

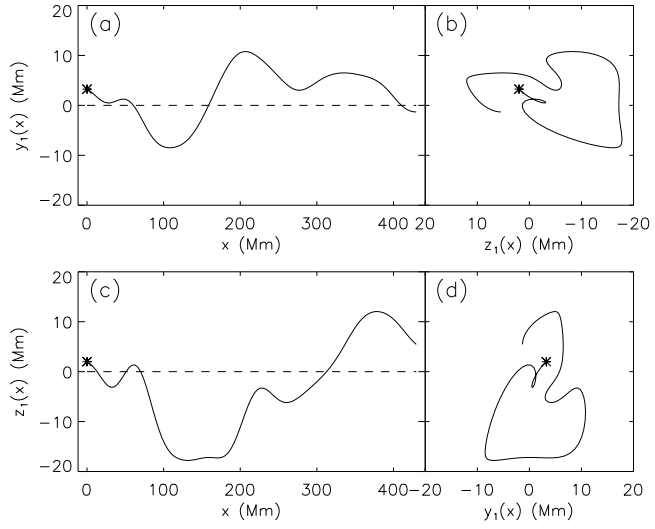

FIG. 3.—Axis of a flux tube at a depth of $z = 160$. The horizontal (*a*) and vertical (*c*) perturbations are plotted against x. The same tube is shown in y_1-z_1 projection in (*b*) and (*d*). From the point at $x = 0$ (*asterisk*) these curves progress roughly counterclockwise, indicating a positive writhe.

TABLE 1

SUMMARY OF THE SIGNS (L±) OF VARIOUS QUANTITIES ASSOCIATED WITH TWIST AND HELICITY AND THE HANDEDNESS (R OR L) OF HELICAL FIELD LINES[a]

Quantity	North Solar Hemisphere	South Solar Hemisphere
$\langle \boldsymbol{u} \cdot \nabla \times \boldsymbol{u} \rangle$	−	+
α	+	−
Im $\langle \tilde{v}_k^e \tilde{w}_k^{e*} \rangle$	+	−
Flux tube axis.....	R	L
Joy's law.....	R	L
$\langle \Sigma_0 \rangle$	−	+
J_ℓ / B_ℓ	−	+
$\alpha_{\rm pcm}$	−	+

[a] The signs reflect the Coriolis effect on turbulence in the bulk of the CZ; rising, expanding material will develop retrograde rotation, while sinking, contracting material will develop prograde rotation. Some theoretical studies indicate that several of these signs are reversed in a layer near the bottom of the CZ. None of the signs is expected to change with solar cycle.

internal fluid motions (i.e., eq. [12]). As in all thin-flux tube models (Spruit 1981) we lack a self-consistent mechanism for maintaining the form of the assumed fluid motion. (Interestingly, Bhattacharjee & Yuan 1995 have proposed an internal "hyper-resistivity" mechanism that drives "internal" flows in the presence of a strong magnetic field. It conserves helicity and can produce chirality of either sign. Further investigation might shed light on possible relations of this to the Σ-effect.)

The α-effect is most frequently invoked in magnetic dynamo models, where it amplifies existing magnetic flux. The Σ-effect does not change the flux Φ of the flux tube, which is constant by hypothesis. Thus, the Σ-effect cannot generate the observed magnetic flux. Rather, it may reconfigure the flux that is generated below the CZ, quite possibly by the α-effect itself. While much work has been done on the efficacy of the α-effect in this generation process, it would seem to have the wrong sign to explain the handedness of the emergent field.

4. CONVECTIVE TURBULENCE MODEL

4.1. *Properties of the Turbulence*

We wish to estimate the expected magnitude of the Σ-effect on a rising flux tube. During its rise, this flux tube is acted on by the turbulent velocity field of the solar CZ. We model this velocity field by generating $\tilde{v}^e(x, t)$ and $\tilde{w}^e(x, t)$ as random functions whose properties reflect those expected of turbulence in a rotating frame. As in LF we use the mixing-length formalism as a guide.

For homogeneous turbulence the correlation between different components of the velocity spectrum is characterized by the tensor $\Phi_{ij}(\boldsymbol{k})$

$$\langle u_i^e(\boldsymbol{k}) u_j^{e*}(\boldsymbol{k}') \rangle = \Phi_{ij}(\boldsymbol{k}) \delta(\boldsymbol{k} - \boldsymbol{k}') \, . \tag{37}$$

If the turbulence is incompressible and isotropic but not mirror symmetric then the tensor Φ_{ij} has the general form

$$\Phi_{ij}(\boldsymbol{k}) = \frac{E(k)}{4\pi k^2} (\delta_{ij} - \hat{k}_i \hat{k}_j) + \frac{iF(k)}{8\pi k^3} \epsilon_{ijs} \hat{k}_s \tag{38}$$

(Moffatt 1978), where δ_{ij} is the Kronecker delta, ϵ_{ijs} is the Levi-Civita symbol, and $\hat{k}_i$ is the ith component of the unit vector $\hat{\boldsymbol{k}} = \boldsymbol{k}/k$. While homogeneity, isotropy and incompressibility are routinely assumed in the theoretical investigation of turbulence, they do not obviously apply to the solar CZ. Quite remarkably, however, some numerical simulations suggest that the most anisotropic elements are strong down flows that occupy only a small fraction of the CZ volume. The remainder of the volume, and thus the majority of the CZ, contains turbulence of a largely isotropic nature (Stein & Nordlund 1989; Cattaneo et al. 1991). This isotropic turbulence contains scales equal to or smaller than the scale height and therefore can be considered approximately incompressible. In light of these facts, and because it simplifies the model considerably (i.e., permitting Fourier analysis), we use the homogeneous, isotropic, incompressible turbulence expression of equation (38).

The functions $E(k)$ and $F(k)$ are called the energy spectrum and helicity spectrum. They are defined such that their integrals give the total energy (per unit mass) and the kinetic helicity, respectively,

$$\tfrac{1}{2} \langle | \boldsymbol{u}^e(\boldsymbol{x}) |^2 \rangle = \tfrac{1}{2} \int \Phi_{ii}(\boldsymbol{k}) d\boldsymbol{k} = \int_0^\infty E(k) dk \, , \tag{39}$$

$$\langle \boldsymbol{u}^e \cdot \nabla \times \boldsymbol{u}^e \rangle = - \int i k_r \epsilon_{irj} \Phi_{ij}(\boldsymbol{k}) d\boldsymbol{k} = - \int_0^\infty F(k) dk \tag{40}$$

(repeated indices are summed over). If defined according to equation (38) the sign of $F(k)$ is opposite to the kinetic helicity (Moffatt 1978 gives this sign incorrectly; this error seems to have been propagated in the literature).

For the spectrum of CZ turbulence we will adopt a simple model we call the *shell model*. At any given depth the turbulence is taken to be homogeneous, isotropic, and incompressible and to be characterized by the local mixing-length velocity $v_{\rm m.l.}$ and mixing length $l_{\rm m.l.}$. Furthermore, the spectrum is taken to be a monochromatic spherical shell in wavenumber space; all motions are strictly at the mixing length. Thus, the energy spectrum is given by

$$E(k) = \tfrac{3}{2} v_{\rm m.l.}^2 \, \delta(k - k_{\rm m.l.}) \, , \tag{41}$$

where $k_{\rm m.l.} \equiv 2\pi / l_{\rm m.l.}$. The factor of $\frac{3}{2}$ arises from our interpretation that the mixing length velocity $v_{\rm m.l.}$ represents the rms velocity in *one direction* only: $v_{\rm m.l.}^2 = \langle (w^e)^2 \rangle$. The helicity spectrum will be taken to be

$$F(k) = 3h v_{\rm m.l.}^2 \, k_{\rm m.l.} \, \delta(k - k_{\rm m.l.}) \, , \tag{42}$$

where h is a dimensionless parameter. Realizability requires that $|F(k)| \leq 2kE(k)$ (Moffatt 1978), which places the constraint $|h| \leq 1$. The kinetic helicity of the turbulence is therefore

$$\langle \boldsymbol{u}^e \cdot \nabla \times \boldsymbol{u}^e \rangle = -3h v_{\rm m.l.}^2 \, k_{\rm m.l.} \, . \tag{43}$$

The parameter h reflects the kinetic helicity in the turbulence, thus it should reflect the influence of the Coriolis force.

The correlations between the driving functions $\tilde{v}_k^e$ and $\tilde{w}_k^e$ can be found by integrating the three-dimensional spectra over k_y and k_z. For the continuous wavevectors this gives

$$\langle u_i^e(k_x) u_j^{e*}(k_x') \rangle = \delta(k_x - k_x') \int \Phi_{ij}(\boldsymbol{k}) dk_y \times dk_z \to \delta'_{k_x, k_x} \Delta k_x \int \Phi_{ij}(\boldsymbol{k}) dk_y \, dk_z \, ,$$

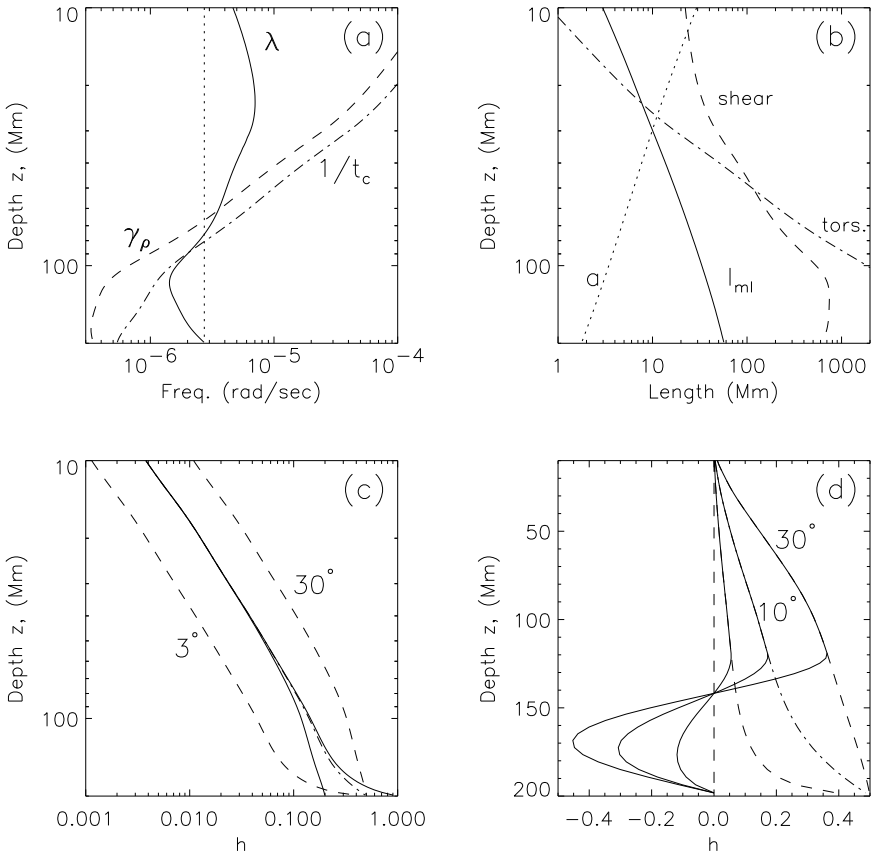

FIG. 4.—Characteristics of the rising flux tube as a function of depth z, plotted vertically with the top ($z = 0$) at the top of the plots. (*a*) Characteristic frequencies: λ (*solid line*), γ_ρ (*dashed line*), $1/t_c$ (*dot-dashed line*), and 2 $\Omega_\odot$ sin 30° (*dotted line*). (*b*) Characteristic lengths in megameters: $l_{\rm m.l.}$ (*solid line*), a (*dotted line*), and the critical damping lengths for shear and torsional Alfvén waves ($2\pi/k_{{\rm cr},\perp}$: *dashed line*; $2\pi/k_{{\rm cr},\rho}$: *dot-dashed line*, respectively). (*c*) Kinetic helicity coefficient $h(z)$ for model H with $\bar{h} = 0.5$ and $\theta = 10°$ (*dot-dashed line*). Also shown are $\bar{h} = 0.2$, 1 at $\theta = 10°$ (*solid line*) and $\theta = 3°$, 30° with $\bar{h} = 0.5$ (*dashed line*). (*d*) Comparison with model B (*solid line*) for $\bar{h} = 0.5$, at $\theta = 3°$, $\theta = 10°$, and $\theta = 30°$. Note that this uses linear axes. Broken and dashed lines correspond to the same curves in (*c*).

where the final expression is the version for discrete spectral modes separated by Δk_x. Performing the integral for the cases of $i = j = 2$ and $i = j = 3$ gives

$$\langle \tilde{v}_k^e \tilde{v}_{k'}^{e*} \rangle = \langle \tilde{w}_k^e \tilde{w}_{k'}^{e*} \rangle = \frac{3v_{\rm m.l.}^2}{8k_{\rm m.l.}} \left(1 + \frac{k^2}{k_{\rm m.l.}^2}\right) \times \Delta k \delta_{k,k'} , \quad |k| \le k_{\rm m.l.} , \tag{44}$$

where the index k is used for k_x to correspond to the notation from the remainder of the paper. LF did not assume incompressible turbulence and found a slightly different correlation; the discrepancy in the final results is approximately 10%. Note that even though the homogeneous turbulence is localized to the wavenumber $|\boldsymbol{k}| = k_{\rm m.l.}$, when the spectrum is projected onto the k_x-axis there is energy at all lower wavenumbers.

The case where $i = 2$ and $j = 3$ gives the correlation between velocity components

$$\langle \tilde{v}_k^e \tilde{w}_{k'}^{e*} \rangle = \frac{3ihv_{\rm m.l.}^2 k}{4k_{\rm m.l.}^2} \Delta k \, \delta_{k,k'} , \quad |k| \le k_{\rm m.l.} . \tag{45}$$

These correlations are the properties characterizing the turbulent velocity fields that are relevant to the rising flux tube.

Appendix B describes the algorithm for generating pseudorandom functions $\tilde{v}_k^e(t)$ and $\tilde{w}_k^e(t)$ satisfying the above properties. These functions are used as inputs for the axis evolution equations (9a) and (9b), whose solutions are used, in turn, as inputs for the twist evolution equations (13) and (14). The properties of the random functions depend on the local values of $k_{\rm m.l.}$, $v_{\rm m.l.}$, and h, which are discussed below.

4.2. *Properties of the Convection Zone*

The parameters $k_{\rm m.l.}$ and $v_{\rm m.l.}$ are standard features of mixing length theory. We take these, and other atmospheric functions of depth, from the CZ model given by Spruit (1974) because this same model has been used in several previous theoretical investigations (Fan, Fisher, & DeLuca 1993; Fan, Fisher, & McClymont 1994; LF). LF compared their results when a different CZ model was used and found little difference.

The kinetic helicity of CZ turbulence is not as well understood theoretically. To assign a value to the parameter h we reason as follows. Kinetic helicity in CZ turbulence arises through the action of Coriolis forces on upwelling-expanding or downflowing-contracting gas. If the rotation were absent, or the upwelling did not interact with it, the fluid motion would not be helical. Thus, at solar latitude θ we expect $h \sim \Omega_\odot \sin(\theta)$; it is positive in the northern hemisphere. For the Coriolis force to be effective, the rotation timescale must be smaller than the eddy timescale (when this is not the case, as it is not in an ordinary bathtub, the Coriolis force has negligible effect). In CZ turbulence the

eddy turnover time is $t_{\rm m.l.} \equiv 1/(v_{\rm m.l.} k_{\rm m.l.})$. Thus, we look for $h \sim 2t_{\rm m.l.}\Omega_\odot \sin(\theta) \equiv \mathrm{Ro}^{-1}$, the inverse of the Rossby number (Zeldovich, Ruzmaikin, & Sokoloff 1983). Finally, even when completely dominated by rotation it is not possible for h to exceed unity. Placing an upper bound of $\bar{h} \leq 1$ we propose a simple form we call model H:

$$h = \frac{\bar{h}\mathrm{Ro}^{-1}}{\sqrt{\bar{h}^2 + \mathrm{Ro}^{-2}}} . \tag{46}$$

This model endows the kinetic helicity with the following limiting forms (Zeldovich et al. 1983):

$$\langle \boldsymbol{u}^e \cdot \nabla \times \boldsymbol{u}^e \rangle = \begin{cases} -2v_{\rm m.l.}\Omega_\odot \sin(\theta) , & \mathrm{Ro}^{-1} \ll 1 . \\ -\bar{h} v_{\rm m.l.}^2 k_{\rm m.l.} \operatorname{sgn}(\theta) , & \mathrm{Ro}^{-1} \gg 1 . \end{cases} \tag{47}$$

Several numerical simulations of compressible turbulence in a rotating atmosphere have shown a kinetic helicity that changes sign near the bottom boundary (Glatzmaier 1985; Brandenburg et al. 1990). This is attributed to the horizontal expansion of descending material encountering a lower boundary. In particular, Brandenburg et al. found that

$$\frac{\langle \boldsymbol{u}^e \cdot \nabla \times \boldsymbol{u}^e \rangle}{2\Omega v_{\rm m.l.}}$$

was roughly sinusoidal with depth over the single density scale height of their simulation. To mimic this behavior we propose model B

$$h(z) = \frac{\bar{h}\mathrm{Ro}^{-1}}{\sqrt{\bar{h}^2 + \mathrm{Ro}^{-2}}} \times \begin{cases} \sin\{\ln[\rho(z)/\rho_0]\} , & \rho(z) \geq e^{-1}\rho_0 , \\ 1 , & \rho(z) < e^{-1}\rho_0 , \end{cases} \tag{48}$$

where $\rho_0 = \rho(Z_0)$ is the density at the base of the convection zone. This form is chosen to provide a layer, one density scale height deep, in which the kinetic helicity has the sign opposite to that characteristic of the hemisphere.

We will explore the efficacy of the Σ-effect in turbulence characterized by both model H and model B, with a range of values of $\bar{h}$. Model H has the advantage of being straightforward and having fewer ad hoc elements. Model B contains a layer of reverse kinetic helicity that is theorized to exist in the solar CZ. It would seem that this layer might affect the amount of twist imparted to the flux tube and perhaps even change its sign. In fact, we will find that choice of model and choice of $\bar{h}$ have very little effect on the final twist. For this reason, we will limit our consideration to these two models and one free parameter.

The properties of the model CZ are summarized in Figure 4. This depicts a flux tube with $\Phi = 10^{21}$ Mx and $B_0 = 30$ kG. The different helicity models are compared in Figures 4*c* and 4*d*. Note that Ro^{-1} increases rapidly at the very bottom where the eddy turnover time increases. In almost all cases this is the only place that $\bar{h}$ comes into effect. The bottom density scale height spans the depths 119 Mm $< z <$ 200 Mm; this is where model B differs from model H.

5. RESULTS OF THE MODEL

5.1. *The Numerical Calculations*

The implementation of the above model proceeds as follows. First, the parameters are set, consisting of Φ, B_0, the latitude θ, and the kinetic helicity model (H or B) with its parameter $\bar{h}$. All runs use an initial magnetic field strength $B_0 = 30$ kG, since this has been found to be reasonable in other simulations (Fan et al. 1993; LF).

The zero-order rise is solved up to a minimum depth Z_f. We adopt a value $Z_f = 30$ Mm, since beyond this the radius of the flux tube makes thin equations unlikely to be valid.

The equations of the first-order axial evolution equations (9a) and (9b) are solved using the zeroth-order solution and a single realization of the random functions $\tilde{v}_k^e(t)$ and $\tilde{w}_k^e(t)$. This realization is generated using the algorithm described in Appendix B, which uses a pseudorandom number generator. Integration of equations (9a) and (9b) results in Fourier coefficients $y_k^{(1)}$ and $z_k^{(1)}$ at depth Z_f. The superscript here indicates that these are but a single realization of the random fields. An example of these solutions is shown in Figure 3.

These first-order equations are then solved repeatedly using different realizations of $\tilde{v}_k^e(t)$ and $\tilde{w}_k^e(t)$ each time. This gives N different values for each Fourier coefficient, e.g., $y_k^{(i)}$, $i = 1, 2, \ldots, N$, which can be used to estimate ensemble averages, e.g.,

$$\langle |y_k|^2 \rangle \simeq \langle\langle |y_k|^2 \rangle\rangle_N \equiv \frac{1}{N} \sum_{i=1}^{N} |y_k^{(i)}|^2 . \tag{49}$$

The calculated average $\langle\langle \cdots \rangle\rangle_N$ is only an approximation to the theoretical ensemble average $\langle \cdots \rangle$. The approximation naturally improves as the sample size N is increased.

Each realization of the tube axis, $y_k^{(i)}(t)$, $z_k^{(i)}(t)$, is then used to find $\Sigma_k^{(i)}(t)$ in the twist equations (25a) and (25b). Integrating these equations gives a realization of the tube's twist, $q_k^{(i)}$, and spin, $\omega_k^{(i)}$. The first of these can be used to estimate the mean twist $\langle q_0 \rangle$. This quantity can also be estimated using purely axial information

$$\langle q_0 \rangle \simeq \langle\langle q_0 \rangle\rangle_N \simeq -\sum_k k^3 \operatorname{Im}(\langle\langle y_k z_k^* \rangle\rangle_N) . \tag{50}$$

These two estimates for $\langle q_0 \rangle$ are found to agree very well.

The value of $\langle q_0 \rangle$ changes during rise according to equation (27). Figure 5 shows the values of $\langle\langle q_0 \rangle\rangle_N$ and $\langle\langle \Sigma_0 \rangle\rangle_N$ as a function of depth z (increasing downward). The runs were done for $\Phi = 3 \times 10^{21}$ Mx, $B_0 = 30$ kG, $\theta = 10°$, and a turbulence of model H with $\bar{h} = 0.2$. The

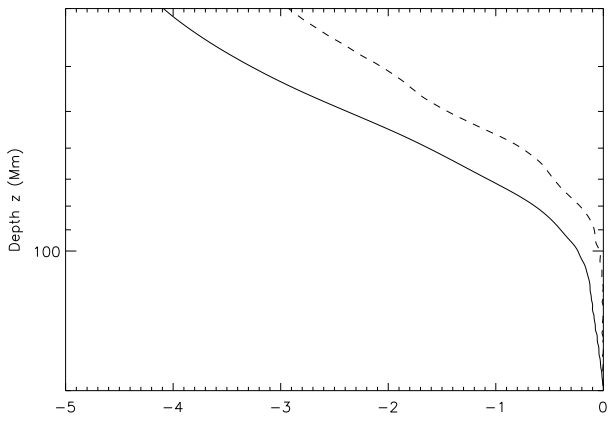

FIG. 5.—Evolution of twist for a flux tube with $\Phi = 3 \times 10^{21}$ Mx, at $\theta = 10°$ latitude. Turbulence is generated with model H and $\bar{h} = 0.2$. The averages are estimated from $N = 1000$ runs. Shown are $\langle\langle q_0 \rangle\rangle_N$ (*solid line*) in units of 10^{-3} Mm^{-1} and $\langle\langle \Sigma_0 \rangle\rangle_N$ (*dashed line*) in units of 10^{-8} Mm^{-1} s^{-1}.

averages are based on $N = 1000$ realizations. Both quantities increase slowly in the lower half of the CZ and much more rapidly thereafter. At the depth $z = Z_f = 30$ Mm, where the simulation is stopped, $\langle\langle q_0\rangle\rangle_N = -4.1 \times 10^{-3}$ Mm^{-1}.

The mean twist at a position x along the tube is found from averaging its Fourier expansion

$$\langle q(x)\rangle = \sum_k \langle q_k\rangle e^{ikx} = \langle q_0\rangle$$

since $\langle q_k\rangle = 0$ for $k \neq 0$. The typical departure from this mean is characterized by the *dispersion* Δq

$$(\Delta q)^2 \equiv \langle q^2(x)\rangle - \langle q(x)\rangle^2 = \sum_k \langle |q_k|^2\rangle - \langle q_0\rangle^2 \,. \quad (51)$$

There is an intrinsic dispersion Δq in the twist because of the statistical nature of the Σ-effect; it is not an error.

Figure 6 shows numerical estimates of each of the spectra for the tube from Figure 5. Raw averages, such as $\langle |y_k|^2\rangle$, depend on the spacing of wavenumbers $\Delta k = 2\pi/L$, where L is the length of the horizontal tube. (In all the runs here $L = 1200$ Mm, but this is not relevant to the results. See the discussion in § 4.1 of LF). We plot spectral densities such as

$$\frac{\langle\langle |y_k|^2\rangle\rangle_N}{\Delta k} \,,$$

which are independent of L. A sum of $\langle\langle |y_k|^2\rangle\rangle_N$ over k then corresponds to an integral of the density over a continuous wavenumber k.

Figure 6*a* shows the spectral energy densities of the axial perturbations

$$\frac{k^2\langle\langle |y_k|^2\rangle\rangle_N}{\Delta k} \,, \quad \frac{k^2\langle\langle |z_k|^2\rangle\rangle_N}{\Delta k} \,,$$

as reported by LF. The vertical perturbations ($\langle\langle |z_k|^2\rangle\rangle_N$) are larger because of the higher drag in equation (9b); their density is the higher curve. Figure 6*b* shows the correlation density

$$\frac{k^3 \,\mathrm{Im}\,(\langle\langle y_k z_k^*\rangle\rangle_N)}{\Delta k}$$

in the lower curve. The integral of this curve gives the estimate of $\langle\langle q_0\rangle\rangle_N = -4.1 \times 10^{-3}$ Mm^{-1} from the last expression in equation (50). The upper curve shows the theoretical maximum of this quantity

$$\frac{k^3\langle\langle |y_k|^2\rangle\rangle_N^{1/2}\langle\langle |z_k|^2\rangle\rangle_N^{1/2}}{\Delta k} \quad (52)$$

for comparison. A ratio of the two curves gives the degree of correlation between the perturbations

$$\frac{\mathrm{Im}\,(\langle\langle y_k z_k^*\rangle\rangle_N)}{\langle\langle |y_k|^2\rangle\rangle_N^{1/2}\langle\langle |z_k|^2\rangle\rangle_N^{1/2}} \,,$$

which is at the level of $\simeq 9\%$ here.

Figures 6*c* and 6*d* show the spectral densities of the source and the twist

$$S_\Sigma(k) \equiv \frac{\langle\langle |\Sigma_k|^2\rangle\rangle_N - \langle\langle \Sigma_0\rangle\rangle_N^2 \,\delta_{k,0}}{\Delta k} \,, \quad (53)$$

$$S_q(k) \equiv \frac{\langle\langle |q_k|^2\rangle\rangle_N - \langle\langle q_0\rangle\rangle_N^2 \,\delta_{k,0}}{\Delta k} \,, \quad (54)$$

respectively. According to equation (51) the integral of $S_q(k)$ provides an estimate of the scatter. Here we find that $\Delta q \simeq 5.0 \times 10^{-2}$ Mm^{-1} is approximately 10 times larger than the mean $\langle q_0\rangle$.

The numerical estimate $\langle\langle q_0\rangle\rangle_N$ has an error σ_q, which decreases for increasing sample size N. Denoting by K the half-width at half-maximum of the main peak in $S_q(k)$, we

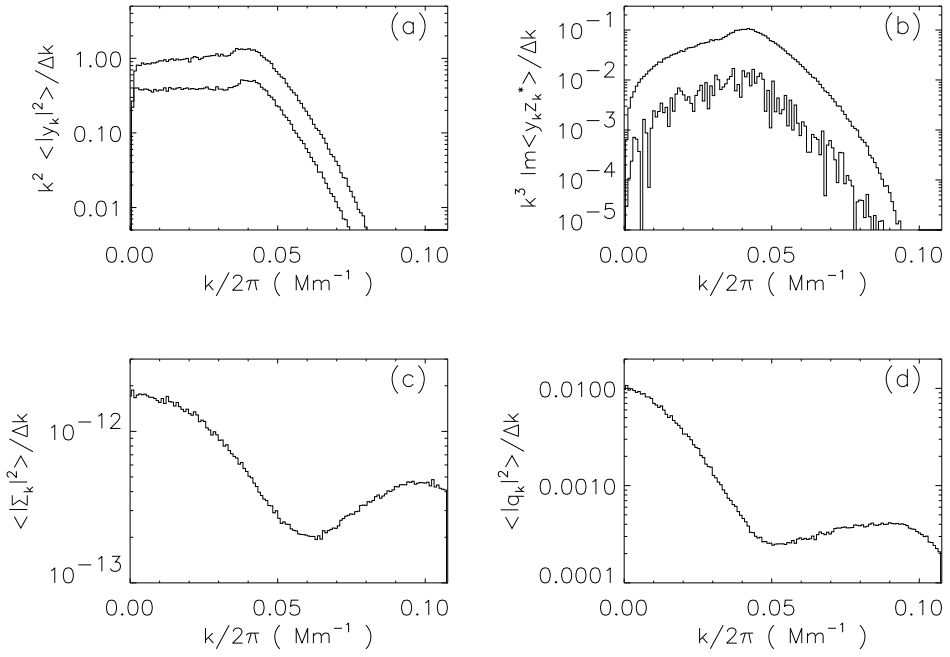

FIG. 6.—(*a*) Axial energies $k^2\langle |y_k|^2\rangle/\Delta k$ (*bottom line*) and $k^2\langle |z_k|^2\rangle/\Delta k$ (*top line*). (*b*) The cross correlation $k^3\mathrm{Im}\langle y_k z_k^*\rangle/\Delta k$ (*bottom line*) and its theoretical maximum (*top line*) from eq. (52). (*c*) The spectral density $S_\Sigma(k)$ of the source term. (*d*) The spectral density $S_q(k)$ of the twist.

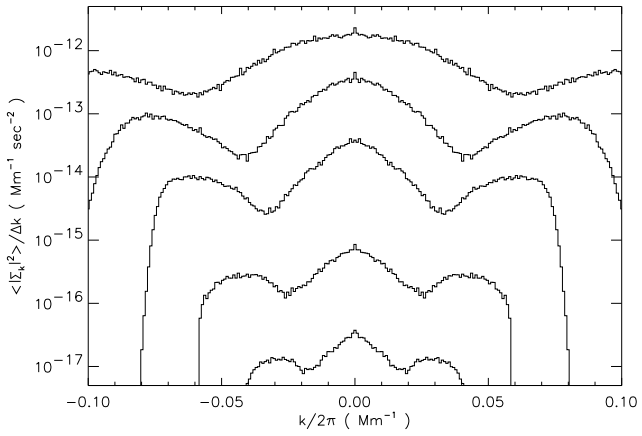

FIG. 7a

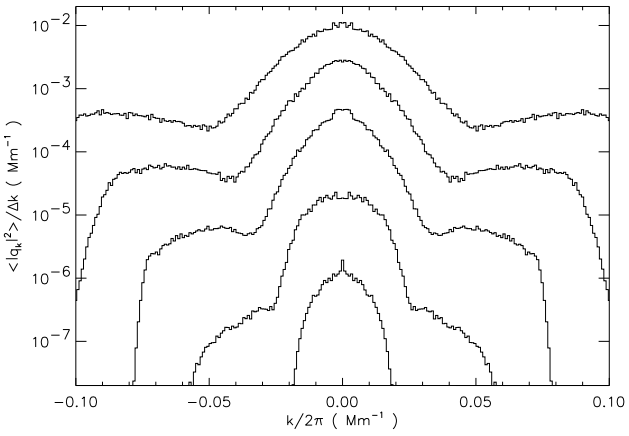

FIG. 7b

FIG. 7.—Spectral densities (*a*) $S_\Sigma(k)$ and (*b*) $S_q(k)$ during the rise of the tube. The tube is the same as in Fig. 6. The curves represent the depths, from bottom to top, $z = 150$, 100, 70, 50, and 30 Mm.

can estimate the error as

$$\sigma_q \equiv \left(\frac{\langle\langle q_0^2\rangle\rangle_N - \langle\langle q_0\rangle\rangle_N^2}{N-1}\right)^{1/2} \simeq \frac{1}{\sqrt{N}}\left(\frac{\Delta k}{K}\right)^{1/2}\Delta q\ . \tag{55}$$

This is smaller than the intrinsic dispersion Δq because the N runs represent multiple independent samples of the twist $q(x)$. The twist is correlated with a length $\ell_k = 2\pi/K$ so each tube contains $L/\ell_k = K/\Delta k$ independent samples of the twist. N independent flux tubes then give an estimate of $\langle q_0\rangle$ with the error σ_q above. For the run being considered $\sigma_q \simeq 2 \times 10^{-4}$ Mm^{-1}, which is 5% of the mean.

The shape of the twist spectrum $S_q(k)$ reflects that of its source $S_\Sigma(k)$. The nature of the relation is further elucidated by plotting the spectral densities at increasing depths z (Fig. 7). This reveals that the source function increases in magnitude as the tube rises. The twist spectrum also grows as the tube rises.

5.2. *Variation of Parameters*

Simulations of the nature described above are conducted for flux tubes with varying parameters. Each simulation consists of $N = 1000$ realizations yielding errors akin to those just explored. For ready comparison to the observations from PCM, we convert the twist q into "helicity" $\alpha_{\rm pcm}$ using equation (35) to give

$$\langle\alpha_{\rm pcm}\rangle \equiv 2\langle q_0\rangle\ , \quad \Delta\alpha_{\rm pcm} \equiv 2\Delta q\ . \tag{56}$$

First we consider a flux tube whose flux is of typical magnitude $\Phi = 3 \times 10^{21}$ Mx. We use model H with $\bar{h} = 0.2$ and vary the latitude θ. Figure 8 shows $\langle\alpha_{\rm pcm}\rangle$ in units of 10^{-8} m^{-1} for comparison with Figure 1. The statistical errors in each data point are all $2\sigma_q \simeq 0.04 \times 10^{-8}$ m^{-1} (smaller than the diamonds) as in Figure 6. A linear fit (*dotted line*)

$$\langle\alpha_{\rm pcm}\rangle \simeq -5.8 \times 10^{-10}\theta_{\rm deg}\ {\rm m}^{-1}\ , \tag{57}$$

is not within the error bars, indicating that the actual dependence on latitude is only approximately linear. This approximate fit is about twice as large as that observed by PCM (Fig. 1*a*). The power law

$$\langle\alpha_{\rm pcm}\rangle = -3.03 \times 10^{-8}(\sin\theta)^{3/4}\ {\rm m}^{-1} \tag{58}$$

(*dashed line*) more accurately fits the results of the simulations.

The solid lines in Fig. 8 show $\langle\alpha_{\rm pcm}\rangle \pm \Delta\alpha_{\rm pcm}$ defining the expected range of values. The dispersion $\Delta\alpha_{\rm pcm}$ is independent of latitude to within statistical errors. In fact, the spectral densities $S_q(k)$ at each latitude, including $\theta = 0$, are indistinguishable from one another. This is an important and possibly observable feature of the Σ-effect. Each mode q_k is driven by the local turbulence. Its variance reflects the level of turbulence, which is independent of latitude. Only $\langle q_0\rangle$ depends on cross correlations that are latitude dependent.

The next series of runs explores the flux dependence of the Σ-effect. Figure 9*a* shows $|\langle\alpha_{\rm pcm}\rangle|$ for flux tubes of varying fluxes Φ at latitudes of 2°.5, 10°, and 30° (the absolute value is shown since $\langle\alpha_{\rm pcm}\rangle < 0$ in the northern hemisphere). A single fit

$$\langle\alpha_{\rm pcm}\rangle = -5.64 \times 10^{-8}(\sin\theta)^{3/4}\Phi_{21}^{-0.69}\ {\rm m}^{-1}\ , \tag{59}$$

is made to all three curves (Φ_{21} is the flux in units of 10^{21} Mx). This fit includes the latitude dependence from equation (58). Each data point represents $N = 1000$ trials, and the statistical errors are only a significant fraction of the mean at $\theta = 2°.5$. The dispersion $\Delta\alpha_{\rm pcm}$ (*solid line*) depends on Φ but not on latitude.

The final sets of runs explore the dependence on the kinetic helicity model. Figure 9*b* shows the variation in

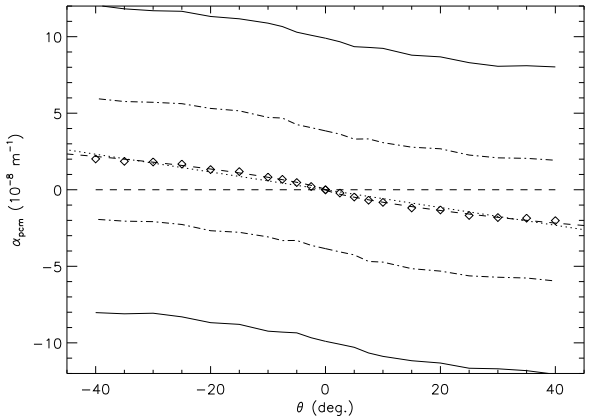

FIG. 8.—Mean helicity $\langle\alpha_{\rm pcm}\rangle$ of a 3×10^{21} Mx flux tube as a function of latitude. Values from simulations are shown as diamonds. Solid lines show $\langle\alpha_{\rm pcm}\rangle \pm \Delta\alpha_{\rm pcm}$ and broken lines show $\langle\alpha_{\rm pcm}\rangle \pm \Delta\bar{\alpha}_{\rm pcm}$ (see eq. [66]). Two fits are shown as dotted and dashed lines.

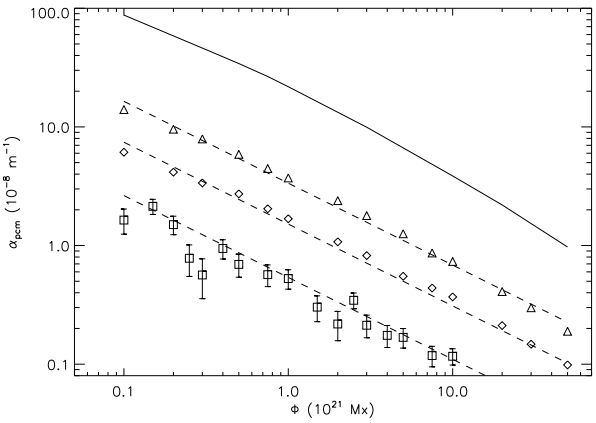

FIG. 9*a*

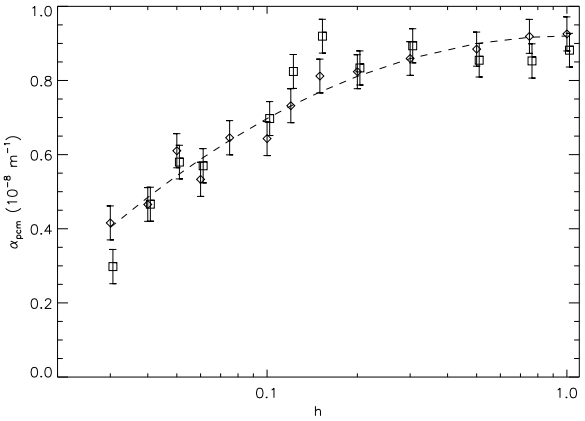

FIG. 9*b*

FIG. 9.—$|\langle\alpha_{pcm}\rangle|$ for various parameters. (*a*) Against flux Φ for model H and $\bar{h} = 0.2$ at latitudes of 2°.5 (*squares*), 10° (*diamonds*) and 30° (*triangles*). Dashed lines are the single fit (eq. [59]). The dispersion $\Delta\alpha_{pcm}$ (*solid line*) does not depend on latitude. (*b*) Against values of $\bar{h}$ for model H (*diamonds*) and model B (*squares*). Dashed line is a fit (eq. [60]). Statistical errors, $2\sigma_q \simeq 0.02 \times 10^{-8}$ m^{-1}, are independent of $\bar{h}$ or model type.

$|\langle\alpha_{pcm}\rangle|$ with $\bar{h}$ for model H (*diamonds*) and model B (*squares*). The flux tube has $\Phi = 3 \times 10^{21}$ Mx and is at a latitude of $\theta = 10°$. The two models are indistinguishable regardless of $\bar{h}$. This may seem remarkable since model B contains the opposite sign of kinetic helicity in the bottom half of the CZ. The top of the CZ, however, contributes almost all of the twist to the tube since the amplitude of the turbulence increases so much with decreasing depth (see, e.g., Fig. 5). A fit to the data,

$$\langle\alpha_{pcm}\rangle = 0.92 \times 10^{-8}[1 - 0.05(\ln\bar{h})^2] \text{ m}^{-1} , \quad (60)$$

is shown primarily as a guide. Note, however, that for $\bar{h} \geq 0.1$ the level of twist does not vary greatly. Because of this low sensitivity we have chosen to forego the investigation of still other models of kinetic helicity in CZ turbulence.

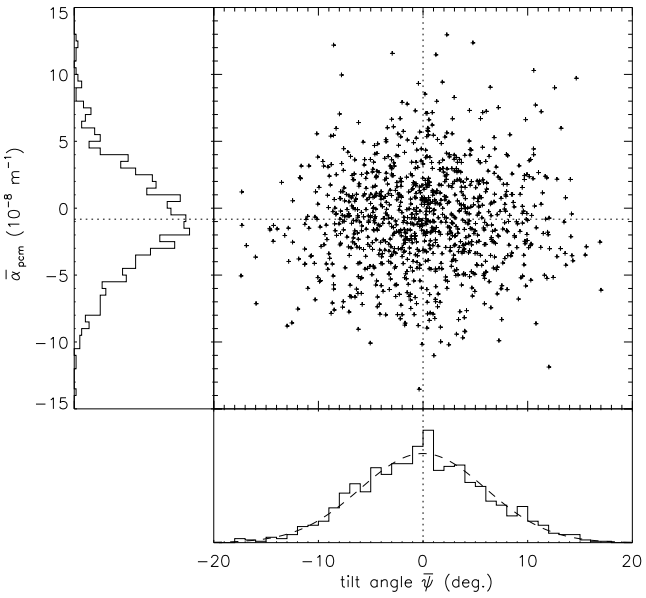

FIG. 10.—Plots of tilt angle $\bar{\psi}^{(i)}$ and twist $\bar{\alpha}^{(i)}_{pcm}$ for $N = 1000$ realizations of a flux tube with $\Phi = 3 \times 10^{21}$ Mx at $\theta = 10°$. Histograms of each variable are shown along the corresponding axis. The mean of each is indicated by a dotted line. The histogram of $\bar{\psi}$ is fit by a Gaussian of width $\Delta\bar{\psi} = 5°.99$.

5.3. *Relation between Twist and Tilt Angle*

The results above show the average properties of the flux tube twist. For each realization it is possible to evaluate α_{pcm} at a single point, say $x = 0$, taken to represent the top of an emerging flux tube (LF)

$$\alpha^{(i)}_{pcm} = 2q(x = 0) = 2\sum_k q^{(i)}_k . \quad (61)$$

The apex of this tube deviates from its mean direction ($\hat{x}$ for the horizontal tube; Joy's law is not present in the model) making a tilt angle ψ

$$\tan\psi^{(i)} = \left.\frac{dy}{dx}\right|_{x=0} = \sum_k iky^{(i)}_k . \quad (62)$$

The arbitrariness of the tube apex ($x = 0$) is necessary because the zeroth-order solution is a horizontal tube rather than an arched Ω-loop with a definite apex.

An idealized active region consists of two points on the photosphere, straddling the apex, separated by a distance d. Following LF we fix d using the empirical relation of Howard (1992)

$$d = d'\Phi_{21} + d_0 , \quad (63)$$

where $d' = 46.6$ Mm and $d_0 = 25.0$ Mm. (For the $\Phi = 3 \times 10^{21}$ Mx flux tube we find $d = 165$ Mm). Taking the poles to be located at $x = \pm d/2$ gives a bipole whose tilt is

$$\tan\bar{\psi}^{(i)} = d^{-1}[y(x = d/2) - y(x = -d/2)]$$
$$= \sum_k iky^{(i)}_k \frac{\sin(kd/2)}{kd/2} . \quad (64)$$

Similarly, we define a mean twist $\bar{\alpha}_{pcm}$ by averaging over the region $-d/2 \leq x \leq d/2$

$$\bar{\alpha}^{(i)}_{pcm} \equiv 2d^{-1}\int_{-d/2}^{d/2} q(x)dx = 2\sum_k q^{(i)}_k \frac{\sin(kd/2)}{kd/2} . \quad (65)$$

It can be quickly verified that $\langle\bar{\alpha}_{pcm}\rangle = \langle\alpha_{pcm}\rangle$, however, the dispersion in $\bar{\alpha}_{pcm}$ will be less than that in α_{pcm},

$$(\Delta\bar{\alpha}_{pcm})^2 = 2\sum_k \langle|q_k|^2\rangle\left[\frac{\sin(kd/2)}{kd/2}\right]^2 , \quad (66)$$

as shown by the broken lines in Figure 8.

Each realization of the turbulent velocity results in values of $\bar{\psi}^{(i)}$ and $\bar{\alpha}^{(i)}_{\rm pcm}$. Figure 10 is a scatter plot showing $N = 1000$ realizations of a tube with $\Phi = 3 \times 10^{21}$ Mx at $\theta = 10°$, using model H with $\bar{h} = 0.2$. The tilt angles have a Gaussian distribution with width $\Delta\bar{\psi} = 5.°99$ about a mean of $\langle\bar{\psi}\rangle = 0.0$, consistent with LF (in LF the tilt angle $\bar{\psi}$ is lamentably denoted by α). The twists are distributed about a mean of $\langle\alpha_{\rm pcm}\rangle = -0.82 \times 10^{-8}\ {\rm m}^{-1}$ with the dispersion of $\Delta\bar{\alpha}_{\rm pcm} = 3.81 \times 10^{-8}\ {\rm m}^{-1}$. The histogram on the left can be directly compared to Figure 1*b* in which $\Delta\alpha_{\rm pcm} = 1.28 \times 10^{-8}\ {\rm m}^{-1}$.

The individual tilts and twists, $\bar{\psi}^{(i)}$ and $\bar{\alpha}^{(i)}_{\rm pcm}$, appear completely uncorrelated with one another. Spearman's rank order correlation test yields $\rho = 0.02$, which is consistent with uncorrelated data at a 49% confidence level. In an actual flux tube the apex will tilt because of Coriolis force, giving rise to a mean $\langle\bar{\psi}\rangle \neq 0$ consistent with Joy's law. This mean will naturally depend on latitude, as does $\langle\bar{\alpha}_{\rm pcm}\rangle$. Thus, the tilt angle and measured twists will be correlated by the mutual dependence of their mean values on latitude. Each of these variables exhibits significant scatter in addition to their mean values. The model above indicates that the scatter will be uncorrelated. Recent analysis of the PCM data set provides a preliminary indication that this may be the case (Pevtsov & Canfield 1998).

6. DISCUSSION

This work has presented a mechanism by which twist can be introduced into an isolated subphotospheric flux tube. A helical deformation of the tube's axis (writhe) will cause the field lines within the tube to twist about the axis in the opposite sense. This is a geometric consequence of the conservation of magnetic helicity and has been noted by previous investigators (Berger & Field 1984; Moffatt & Ricca 1992; LK). Here we note that the handedness of the twist, and not of the writhe, determines the sign of $\alpha_{\rm pcm}$ since the electric current depends on the curl of the field.

The Coriolis effect helically deforms the flux tube axis directly on the large scale characteristic of the CZ depth. This deformation is manifest in the bipolar tilt angle described by Joy's law. In addition, turbulence of the CZ can introduce helical deformation on small scales (at the mixing length) if the turbulence contains a nonvanishing kinetic helicity; we call this the Σ-effect. Both of these helical deformations will be of the handedness appropriate to explain the twist observed by PCM. This sense is opposite to that of the well-known α-effect, which therefore must disagree with these observations.

We believe that small-scale helical deformations, due to convective turbulence, are the most significant source of twist in active region flux tubes. The source term for magnetic twist, Σ in equation (16), involves three spatial derivatives, so it will be dominated by small scales. As further evidence, the measurements of $\alpha_{\rm pcm}$ show a large statistical dispersion (larger than the measurement errors), suggesting a turbulent or random origin.

We have performed a simple calculation to estimate the amount of twist the Σ-effect may produce. This involved a straight horizontal tube that is distorted by turbulent velocities as it rises through the CZ. The distortions are treated as small perturbations. These assumptions are made to simplify the calculation and give a first estimate of this new phenomenon. The model *does* include a back reaction by the Lorentz force, an aspect often omitted from treatments of the α-effect. Furthermore, the turbulent velocity is endowed with a kinetic helicity whose spectrum and amplitude vary with depth.

The results of these simulations indicate that the Σ-effect is significant enough to account for the observed active region twist. Our estimated values of $\langle\alpha_{\rm pcm}\rangle$ and its statistical dispersion $\Delta\bar{\alpha}_{\rm pcm}$ are about twice as large as observed values. Its variation with latitude is consistent with observations. Given the crudeness of the model, this is a very encouraging agreement. It is likely that these values will decrease with some of the improvements to the model; a more realistic turbulence spectrum would distribute the fluctuations more broadly in wavenumber, and an Ω-loop would permit propagation of twist away from the apex.

The model also suggests several signatures of the Σ-effect that might be tested with future observations. First, the mean twist scales inversely with active region flux

$$\langle\alpha_{\rm pcm}\rangle \sim \Phi^{-0.69}\ . \tag{67}$$

Such inverse scaling is common in flux tube models, since larger flux tubes rise more rapidly, providing less time for the actions of turbulence or of the Coriolis force. Similar flux scalings, predicted in ψ and $\Delta\psi$, were confirmed to exist in Wilson sunspot data (Fisher et al. 1995). Second, the dispersion $\Delta\alpha_{\rm pcm}$ is found to be independent of latitude. The dispersion depends on the amplitude of fluctuation induced by the turbulence and not on its correlation properties. Most CZ models predict turbulence whose amplitude does not vary with latitude, even while correlations, such as kinetic helicity, do vary. Finally, fluctuations in $\alpha_{\rm pcm}$ are found to be uncorrelated with fluctuations in tilt angle ψ.

Our model relies on several approximations that are subject to a posteriori verification. As in Longcope & Fisher (LF) we introduced the turbulent velocity $\boldsymbol{u}^e$ as a small perturbation to the drag on the rising tube. This was premised on the assumption $v_{\rm m.l.} \ll v_{\rm ff}$ so that the tube rising through a static atmosphere, at $v_{\rm ff}$, can be used as a lowest order solution. Comparing $v_{\rm ff}(z)$ with $v_{\rm m.l.}(z)$ we find that this scaling holds except near the very bottom of the CZ. It stands to reason that this scaling should hold since the mixing length velocity $v_{\rm m.l.}$ is found from the buoyant free rise of a fluid parcel that exchanges heat much more effectively than the flux tube does (the fluid parcel completely thermalizes over a single scale height, and the flux tube rises essentially adiabatically). After this, we approximate the distortions to the tube, $y_1(x)$ and $z_1(x)$ to be small enough to permit linearization. At least for $y_1(x)$ this is equivalent to making a small angle approximation for the tilt angle ψ as studied by LF. Inspection of Figure 10 reveals that $|\psi| < 15°$ for the medium flux tube ($\Phi = 3 \times 10^{21}$ Mx), well within the scope of the small angle approximation. Since the dispersion scales inversely with flux, $\Delta\psi \sim \Phi^{-3/4}$ (LF), we expect the almost straight approximation to be violated only for smaller flux tubes: $\Phi < 10^{21}$ Mx.

By far the most questionable approximation is the treatment of the lowest order flux tube as perfectly straight instead of as an Ω-loop. The effects of this approximation are investigated in more detail by LF. The apex of an Ω-loop is horizontal, so there is some validity to the model. In truth, however, the approximation was made in order to yield a more tractable model and arrive at preliminary estimates of this new effect. Better estimates of twist due to the Σ-effect will come from using a more accurate treatment of the flux tube. This would almost certainly entail full nonlin-

ear simulations using the full versions of the twist equations (13) and (14). Given the statistical nature of the problem it will be necessary to do $N \sim 1000$ runs at any given parameters.

Further improvements can be sought in more realistic models of CZ turbulence. We have used the shell model because it is simple and because there is little ambiguity in the introduction of kinetic helicity. While more sophisticated models of compressible turbulence have been developed (Canuto & Mazzetelli 1991), these models do not yet include rotation. Without a good model for the helicity spectrum $F(k)$ it would seem to be difficult to improve on the shell model.

The Σ-effect is only one possible mechanism for the introduction of twist. Other investigators have proposed origins such as zonal jets (Rust 1994) or differential rotation. It would be instructive to estimate the magnitudes of $\alpha_{\rm pcm}$ that each such mechanism might produce. Making such quantitative comparisons with observation should discriminate among the models. It has also been proposed that twist is present in a flux tube even before it rises; that twist is produced by the solar dynamo (Longcope, Fisher, & Arendt 1996; Moreno-Insertis & Emonet 1996; Fan, Zweibel, & Lance 1998). Barring great strides in an understanding of magnetic dynamos, the best evidence for this hypothesis may come by eliminating all other mechanisms.

D. W. L. wishes to acknowledge helpful discussions with E. F. Bunn, R. C. Canfield, and M. G. Linton. We thank the staff of the Mees Solar Observatory for observations, the scientific editor, Steven Shore, and the anonymous referee for helpful comments on the manuscript. D. W. L. and A. A. P. were supported by NASA grant NAG 5-5043. Part of the work was done while D. W. L. was visiting UC Berkeley, supported by NSF grant AST 95-28474 and NASA grant NAGW-5133. G. H. F. was supported by NASA grant NAG 5-4181 and NSF grant AST 95-28474, and ATM 96-19441.

APPENDIX A

THE RISE OF A HORIZONTAL FLUX TUBE: THE LOWEST ORDER

The lowest order solution consists of a straight, horizontal ($\hat{\boldsymbol{t}} = \hat{\boldsymbol{x}}$) flux tube rising through a static atmosphere. This was studied in detail by Moreno-Insertis (1983). Below we outline the solution used by LF.

Neglecting inertia, the tube rises at its terminal velocity determined by a balance of upward buoyancy and downward drag:

$$v_{\rm ff} \equiv \left(\left| \frac{\delta\rho}{\rho} \right| \frac{ga\pi}{C_D} \right)^{1/2} . \tag{A1}$$

This terminal velocity depends on the tube's present depth, $z = z_0$, which is itself determined by the rise,

$$\frac{dz_0}{dt} = -v_{\rm ff}(z_0) . \tag{A2}$$

Since the internal and external mass densities are approximately equal ($|\delta\rho| \ll \rho$), the tube's radius is an explicit function of depth, $a(z) = a_0[\rho_0/\rho(z)]^{1/2}$, where a_0 and ρ_0 are the radius and (external) mass density at the beginning of the rise and $\rho(z)$ is the mass density of the local atmosphere.

The tube's relative overdensity, $\delta\rho/\rho$, is determined by instantaneous balance of pressure between the inside and the outside of the tube, $p^e = p^i + B^2/8\pi$, which can be expanded about small differences of density and temperature to give

$$\frac{\delta\rho}{\rho} + \frac{\delta T}{T} + \frac{B^2}{8\pi p(z)} = 0 . \tag{A3}$$

The magnetic field, B, can be found readily from the flux, Φ, and the tube radius, $a(z)$. The temperature difference, δT, will evolve both through the adiabatic expansion of the tube, compared with the superadiabatic temperature gradient of the CZ, and also through thermal diffusion,

$$\frac{d}{dt}\,\delta T = \frac{T(z)}{H_p(z)} (\nabla - \nabla_{\rm ad}) v_{\rm ff}(z) - \frac{1}{\tau_{\rm th}}\,\delta T , \tag{A4}$$

where $\tau_{\rm th}$ is the radiative cooling time for a cylindrical flux tube (Fisher, Chow, & McClymont 1989). For flux tubes larger than 10^{20} Mx this timescale is typically very long and the tube's thermal relaxation is unimportant (Moreno-Insertis 1983; Fisher et al. 1989).

Both equations (A2) and (A4) can be simultaneously integrated in time to yield the entire zeroth-order solution. The external atmosphere determines functions $\rho(z)$, $p(z)$, and so on. These are taken from the model of Spruit (1974) as in LF. The initial temperature difference is specified in terms of the fraction $1 - \epsilon$, by which it counteracts magnetic buoyancy:

$$\delta T(Z_0) = -(1 - \epsilon) T_0 \frac{B_0^2}{8\pi p_0} . \tag{A5}$$

For $\epsilon = 1$ the tube would begin at the same temperature as its surroundings (Moreno-Insertis 1983), while for $\epsilon = 0$ the tube would be in mechanical equilibrium ($\delta\rho = 0$) until the effects of thermal diffusion came into play. All runs use the value $\epsilon = 0.5$.

APPENDIX B

GENERATING THE EXTERNAL VELOCITY FUNCTIONS

To generate the random functions $\tilde{v}^e_k(t)$ and $\tilde{w}^e_k(t)$ we use the algorithm from LF. The velocity functions must each have properties of homogeneous turbulence with moments reflecting the conditions at the present depth. In addition they must be correlated with one another to endow the turbulence with kinetic helicity. As a first step we generate an uncorrelated random, complex function $\xi_k(t)$ and $\eta_k(t)$ through the previous algorithm

$$\xi_k(t) = v_{\text{m.l.}}(t)\mathscr{F}_k[k_{\text{m.l.}}(t)]W_k[\tau(t)] , \tag{B1}$$

$$\eta_k(t) = v_{\text{m.l.}}(t)\mathscr{F}_k[k_{\text{m.l.}}(t)]W'_k[\tau(t)] . \tag{B2}$$

The randomness derives from the complex functions $W_k(\tau)$ and $W'_k(\tau)$, which are independent of one another and are exponentially correlated in their argument

$$\langle W_k(\tau)W^*_k(\tau')\rangle = \exp\left(-|\tau - \tau'|\right) , \tag{B3}$$

and likewise for $W'_k(\tau)$. To produce velocity functions with the local correlation time $t_c(t)$ we define $\tau(t)$ as

$$\tau(t) \equiv \int_0^t \frac{dt'}{t_c(t')} . \tag{B4}$$

Thus, W_k and W'_k are spatial white noise but have a finite correlation time. The real and imaginary parts of each are uncorrelated with one another and have the same distribution.

The spatial structure is provided by the filter function $\mathscr{F}_k(k_{\text{m.l.}})$. This is defined with reference to equation (44) for the shell model

$$|\mathscr{F}_k(k_{\text{m.l.}})|^2 = \frac{3}{8k_{\text{m.l.}}}\left(1 + \frac{k^2}{k^2_{\text{m.l.}}}\right)\Delta k , \quad |k| \le k_{\text{m.l.}} \tag{B5}$$

and vanishes for $|k| > k_{\text{m.l.}}$. This filter function has the property

$$\sum_k |\mathscr{F}_k(k_{\text{m.l.}})|^2 = 1 , \tag{B6}$$

so that the $\sum_k \langle|\xi_k|^2\rangle = v^2_{\text{m.l.}}$. With this filter the average magnitude is

$$\langle|\xi_k|^2\rangle = \frac{3v^2_{\text{m.l.}}}{8k_{\text{m.l.}}}\left(1 + \frac{k^2}{k^2_{\text{m.l.}}}\right)\Delta k , \quad |k| \le k_{\text{m.l.}} . \tag{B7}$$

The complex functions ξ_k and η_k have identical moments but are not correlated with one another. We seek velocities, also with identical moments, but also with the cross correlation

$$\frac{\langle\tilde{v}^e_k\tilde{w}^{e*}_k\rangle}{\langle|\tilde{v}^e_k|^2\rangle} = \frac{2ihk/k_{\text{m.l.}}}{1 + k^2/k^2_{\text{m.l.}}} \equiv i\sin(c_k) , \tag{B8}$$

where c_k is an angle defining the degree of cross correlation. Correlated velocities are constructed by mixing ξ_k and η_k according to the prescription

$$\tilde{v}^e_k = \frac{1}{\sqrt{2}}\left(\xi_k e^{ic_k/2} - \eta_k e^{-ic_k/2}\right) , \tag{B9}$$

$$\tilde{w}^e_k = \frac{1}{\sqrt{2}}\left(\xi_k e^{-ic_k/2} + \eta_k e^{ic_k/2}\right) . \tag{B10}$$

This definition can be seen to give the correlations

$$\langle\tilde{v}^e_k\tilde{v}^{e*}_k\rangle = \langle\tilde{w}^e_k\tilde{w}^{e*}_k\rangle = \langle|\xi_k|^2\rangle ,$$

$$\langle\tilde{v}^e_k\tilde{v}^e_k\rangle = \langle\tilde{w}^e_k\tilde{w}^e_k\rangle = \langle\tilde{v}^e_k\tilde{w}^e_k\rangle = \langle\xi^2_k\rangle = 0 ,$$

$$\langle\tilde{v}^e_k\tilde{w}^{e*}_k\rangle = -\langle\tilde{w}^e_k\tilde{v}^{e*}_k\rangle = i\sin(c_k)\langle|\xi_k|^2\rangle .$$

REFERENCES

Batchelor, G. K. 1967, Fluid Dynamics (Cambridge: Cambridge Univ. Press)
Berger, M. A., & Field, G. B. 1984, J. Fluid Mech., 147, 133
Bhattacharjee, A., & Yuan, Y. 1995, ApJ, 449, 739
Bieber, J. W., Evenson, P., & Matthaeus, W. H. 1987, ApJ, 315, 700
Brandenburg, A., Nordlund, A., Pulkkined, P., Stein, R. F., & Tuomined, I. 1990, A&A 232, 277
Burlaga, L. F. 1988, J. Geophys. Res., 93(A7), 7217
Caligari, P., Moreno-Insertis, F., & Schüssler, M. 1995, ApJ, 441, 886
Canuto, V. M., & Mazzetelli, I. 1991, ApJ, 370, 295
Cattaneo, F., Brummel, N., Toomre, J., Malagoli, A., & Hurlburt, N. E. 1991, ApJ, 370, 282
Choudhuri, A. R., & Gilman, P. A. 1987, ApJ, 316, 788
Chui, A. Y. K., & Moffatt, H. K. 1995, Proc. R. Soc. London A, 451, 609
D'Silva, S., & Choudhuri, A. R. 1993, A&A, 272, 621
Fan, Y., Fisher, G. H., & DeLuca, E. E. 1993, ApJ, 405, 390

Fan, Y., Fisher, G. H., & McClymont, A. N. 1994, ApJ, 436, 907
Fan, Y.-H., Zweibel, E. G., & Lantz, S. R. 1998, ApJ, 493, 480
Ferriz-Mas, A., & Schüssler, M. 1990, in Geophys. Monographs 58, Physics of Magnetic Flux Ropes, ed. C. T. Russel, E. R. Priest, & L. C. Lee (Washington, DC: Amer. Geophys. Union), 141
Fisher, G. H., Chou, D.-Y., & McClymont, A. N. 1989, in Geophys. Monographs 54, Solar System Plasma Physics, ed. J. H. Waite, J. L. Burch, & R. L. Moore (Washington, DC: Amer. Geophys. Union), 47
Fisher, G. H., Fan, Y., & Howard, R. F. 1995, ApJ, 438, 463
Glatzmaier, G. 1985, ApJ, 291, 300
Howard, R. F. 1992, Solar Phys. 142, 233
Jackson, J. D. 1975, Classical Electrodynamics (New York: Wiley)
Klapper, I., & Tabor, M. 1994, J. Phys. A 27(14), 4919
Krause, F., & Rädler, K.-H. 1981, Mean Field Magnetohydrodynamics (New York: Pergamon)
Leka, K. D., Canfield, R. C., McClymont, A. N., & Van Driel-Gesztelyi, L. 1996, ApJ, 426, 547
Longcope, D. W., & Fisher, G. H. 1996, ApJ, 458, 380 (LF)
Longcope, D. W., Fisher, G. H., & Arendt, S. 1996, ApJ, 464, 999
Longcope, D. W., & Klapper, I. 1997, ApJ, 488, 443 (LK)
Martin, S. F., Billamoria, R., & Tracadas, P. W. 1994, in Solar Surface Magnetism, ed. R. J. Rutten, & C. J. Schrijver (Dordrecht: Kluwer), 303
Mickey, D. L. 1985, Solar Phys. 97, 223
Mickey, D. L., Canfield, R. C., LaBonte, B. J., Leka, K. D. Waterson, M. F., & Weber, H. M. 1996, Solar Phys. 168, 229
Moffatt, H. K. 1978, Magnetic Field Generation in Electrically Conducting Fluids (Cambridge: Cambridge Univ. Press)
Moffatt, H. K., & Ricca, R. L. 1992, Proc. R. Soc. London A, 439, 411
Moreno-Insertis, F. 1983, A&A 122, 241
Moreno-Insertis, F., & Emonet, T. 1996, ApJ, 472, L53
Parker, E. 1975, ApJ, 198, 205
Pevtsov, A. A., & Canfield, R. C. 1998, ApJ, submitted
Pevtsov, A. A., Canfield, R. C., & Metcalf, T. R. 1995, ApJ, 440, L109 (PCM)
Rust, D. M. 1994, Geophys. Res. Lett. 21, 241
Rust, D. M., & Kumar, A. 1996, ApJ, 464, L199
Ryutov, D. A., & Ryutova, M. P. 1976, Sov. Phys.–JETP Lett. 43(3), 491
Spruit, H. C. 1974, Solar Phys. 34, 277
———. 1981, A&A 98, 155
Stein, R. F., & Nordlund, Å. 1989, ApJ, 342, L95
Zeldovich, Y. B., Ruzmaikin, A. A., & Sokoloff, D. D. 1983, Magnetic Fields in Astrophysics (New York: Gordon & Breach)
Zirker, J. B., Martin, S. F., Harvey, K. H., & Gaizaukas, V. 1997, Solar Phys. 175, 27